



Available online at [www.sciencedirect.com](http://www.sciencedirect.com)

**ScienceDirect**

Comput. Methods Appl. Mech. Engrg. 378 (2021) 113729

**Computer methods  
in applied  
mechanics and  
engineering**

[www.elsevier.com/locate/cma](http://www.elsevier.com/locate/cma)

# Thermo-elasto-plastic phase-field modelling of mechanical behaviours of sintered nano-silver with randomly distributed micro-pores

Yutai Su<sup>a,b</sup>, Guicui Fu<sup>b</sup>, Changqing Liu<sup>a,\*</sup>, Kun Zhang<sup>a,d</sup>, Liguo Zhao<sup>a</sup>, Canyu Liu<sup>a</sup>, Allan Liu<sup>a</sup>, Jianan Song<sup>a,c</sup>

<sup>a</sup> *Wolfson School of Mechanical, Electrical and Manufacturing Engineering, Loughborough University, Leicestershire LE11 3TU, United Kingdom*

<sup>b</sup> *School of Reliability and Systems Engineering, Beihang University, Beijing 100191, China*

<sup>c</sup> *School of Energy and Power Engineering, Beihang University, Beijing 100191, China*

<sup>d</sup> *MOE Key Laboratory of Pressure Systems and Safety, School of Mechanical and Power Engineering, East China University of Science and Technology, Shanghai 200237, China*

Received 15 December 2020; received in revised form 6 February 2021; accepted 9 February 2021

Available online 1 March 2021

## Abstract

Nano-silver paste is an emerging lead-free bonding material in power electronics, and has excellent mechanical properties, thermal conductivity and long-term reliability. However, it is extremely challenging to model the mechanical and failure behaviours of sintered nano-silver paste due to its random micro-porous structures and the coupled thermomechanical loading conditions. In this study, a novel computational framework was proposed to generate the random micro-porous structures and simulate their effects on mechanical properties and fracture behaviour based on the one-cut gaussian random field model and the thermo-elasto-plastic phase-field model. The elastic modulus, ultimate tensile strength and strain to failure are computed statistically, showing good agreement with the experimental results. Further, the framework was applied to model the fracture of sintered nano-silver paste under thermal cyclic conditions, demonstrating the formation of distinctive crack patterns and complex crack networks. The cracking behaviours observed in the experiments and simulations are remarkably similar to each other. The framework was implemented within Abaqus via a combination of subroutines and Python scripts, automating the process of model generation and subsequent computation. This study provides an efficient and reliable approach to simulate the mechanical and failure behaviours of sintered nano-silver paste with random micro-porous structures.

© 2021 Elsevier B.V. All rights reserved.

**Keywords:** Phase field model; Thermo-elasto-plastic behaviour; Sintered nano-silver; Random micro-porous structure

## 1. Introduction

Nano-silver paste is an emerging lead-free bonding material used as a substitute for Sn/Pb solders in SiC or GaN power electronics, owing to its high melting temperature (961.8 °C), good thermal conductivity (200–300 W/m K) and excellent long-term reliability [1–5]. Due to its high-energy free surface, nano-silver paste can be sintered

\* Corresponding author.

E-mail address: [c.liu@lboro.ac.uk](mailto:c.liu@lboro.ac.uk) (C. Liu).

at a temperature as low as 0.38 T<sub>m</sub> ( $\sim 200$  °C) which is well below the melting point [6–8]. Low temperature sintering process reduces the damage to dies in the power devices or modules, but it also induces inevitable pores in the bonding structures. Despite the improvement of sintering pressure and time, the porous microstructure in the nano-silver paste could not be eliminated and often exhibit stochastic uncertainties, which significantly affect the mechanical strength, thermal conductivity, and fatigue properties of the nano-silver joints [4,9–12].

From the microscopic point of view, micro-porous structure in Ag-particle sintered joint is one of the key issues and extensive research has been conducted to find the quantitative relationships between the porosity and the mechanical behaviour [13–15]. Carr et al. studied the quantitative relationships between the pore fractions and elastic modules through both experiments and simulations. The finite element models were created from the serial block-face scanning electron microscopy images, and the predicted Young's moduli agreed well with the experimental measurements [16]. However, the pore morphologies in the model were fixed, which did not represent the real micro-porous structures. In fact, the sizes and shapes of the pores in the sintered structures have large influences on the mechanical behaviours, and are critical to find the relationships between the porosity and mechanical properties. Yao et al. investigated the effects of varying pore microstructures on the mechanical behaviours of nano-silver porous materials thorough molecular dynamics simulations [17]. Simulation results showed notable difference for pores with morphologies varied among cube, gyroid, sphere and spinodal decomposition, suggesting a dependence of mechanical properties on the microstructural details. More realistic porous structures should be used to substitute those with fixed porosities and regular shapes. Chen et al. characterized the microstructures of the porous ceramic films with different porosities, and reconstructed the three-dimensional microstructures of as-sintered films by focused ion beam (FIB). They also computed the elastic moduli for artificial pore microstructures using cellular automaton method and finite element modelling [18]. Soyarslan et al. modelled three-dimensional stochastic bi-continuous microstructures and the effective elastic properties of the gold-polymer nanocomposites [19]. The Young's moduli and Poisson's ratios could be computed for the generated random bi-continuous composites. Furthermore, Vel and Goupee proposed a multiscale thermo-elastic approach to analyse the properties of random heterogeneous materials, containing random morphology description [20]. Two-phase materials were described by the random morphology description functions, and the mean and deviation of thermo-elastic properties were computed. Based on this random heterogeneous microstructure models, the representative volume element (RVE) could be developed to analyse the macro-scale mechanical properties. In terms of sintered nano-silver paste, Gillman et al. presented an approach for establishing the statistics-property relations of porous microstructures, based on synthetic random porous morphologies generated by gaussian random fields models. In this approach, the two-point probability functions were utilized to characterize the spatial correlations of pore shapes and distributions in the porous structures, showing strong similarities between the real microstructures and the synthetic morphologies [21]. Models with stochastic micro-porous structures could describe the material properties with randomness and statistically evaluate the ranges of the mechanical properties, allowing a better match with the reality.

From a macroscopic perspective, the sintered nano-Ag paste under complex mechanical and thermal conditions shows several cracks between the pores with various shapes and sizes. To analyse this thermo-elasto-plastic porous material, a phase field model is proposed to describe the mechanical behaviours and crack evolutions in the micro-porous structures. Phase field models have been applied extensively to compute the mechanical behaviours and crack propagations of multi-field solids in multi-physical environments, such as elasto-plastic [22], thermo-elastic [23,24], thermo-elasto-plastic [25–27], chemo-mechanical [28], chemo-thermo-mechanical [29], hydro-poro-elastic [30,31] and hydro-poro-elasto-plastic models [32]. Cho et al. utilized the phase field model to describe simultaneous propagations of multiple cracks in the laminated composite, confirming high effectiveness of the approach [33]. Pillai et al. combined the macroscopic theory of porous media and phase-field model within Abaqus, and developed a remarkable approach to predict the crack initiation and propagation in porous materials. Both homogeneous and heterogeneous cases were presented with a consideration of Weibull distribution for solid volume fraction of porous media [34]. However, the simulation results are at macroscopic scale, and did not consider microstructure details. Carlsson and Isaksson showed that the length scale in the phase field method played a key role in determining whether or not the microstructures should be considered [35]. Through both macroscopic and microscopic phase field modelling, the relation between the length scale parameter and the average cell size of the microstructure was numerically studied, and demonstrated that the microscopic models could not be regarded as the homogeneous continuum model when the length scale parameter is smaller than twice the cell size. In general, the pore size of the sintered nano-silver paste is larger than half of the crack length, and the thickness of the sintered layers in power

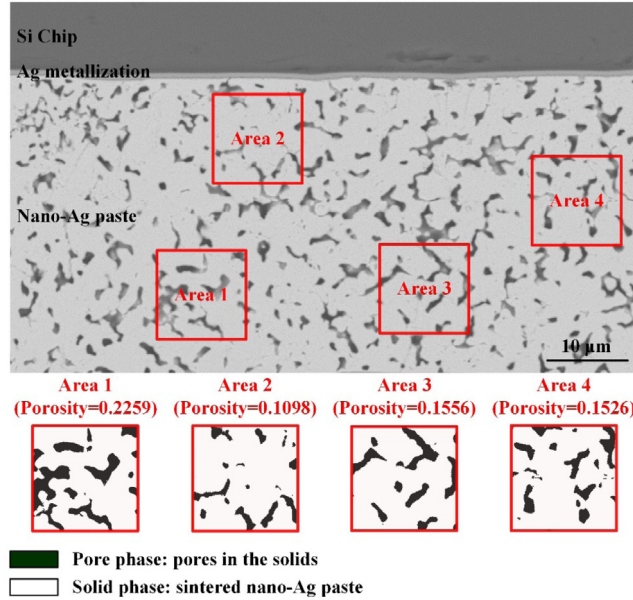


**Fig. 1.** Nano-silver paste micro-porous morphology with pore phase and solid phase.

electronics is too small to homogenize the pores of the nano-silver materials. Therefore, there is a need to consider stochastic microporous morphologies for microscopic phase field modelling of the nano-silver porous materials. Moreover, the sintered nano-silver paste is applied for the high temperature conditions, where elasticity, plasticity and thermal effects should all be considered in the study of crack developments [36–38]. Although Dittmann et al. established the thermo-elasto-plastic models for the porous materials [25,26], they utilized a homogeneous method considering only pore volume fractions, which is not suitable for the sintered nano-silver paste due to the neglect of the random porous microstructure.

This paper aims to develop a thermo-elasto-plastic phase-field model for the sintered nano-silver materials, with explicit consideration of random micro-porous structures. The rest of this paper is organized as follows. In Section 2, the fundamentals for random micro-porous morphology generation are introduced for the sintered nano-silver paste, based on one-cut gaussian random field model and two-point probability function. In Section 3, the phase field model for thermo-elasto-plastic solid is described in detail, including primary fields and state variable definitions, energy functional derivations, governing equations, and spatial and temporal discretization. An implementation scheme of the gaussian random field and the phase field models is given in Section 4 for the sintered nano-silver paste, including porous microstructure characterization, random morphology generation, and the two-layer phase field simulation using Python and Abaqus. Three numerical case studies conducted for the sintered nano-silver material are conducted in Section 5, including uniaxial tensile tests under different temperature, the mechanical and fracture behaviours of the random porous microstructures with specified porosities, and the thermal fatigue failure of sintered nano-silver structure in silicon power modules. Finally, the major conclusions of the paper are given in Section 6.

## 2. Generation of random micro-porous morphology

### 2.1. Microstructural description

Nano-silver paste is a die attach bonding material, consisting of silver nanoparticles and organics. During the sintering process, the silver nanoparticles are interconnected, and the organics are burned out. Micro-porous structure emerges in the sintered nano-silver paste, which could be characterized as a two-phase material composing of silver-solids and micro-pores. The continuously solid phase represents the metal frame, and the connective pore phase represents the micro-pores in the material [39]. The properties of the solid and pore phases are distinctively different. Correspondingly, the features and structure of the pores influence the performance of the two-phase

material. Fig. 1 shows a typical cross-section morphology of nano-silver paste with many connective pores. The porosities in different areas shown in Fig. 1 have clear variations, ranging from 10.98% to 22.59%. The pore shape and size are randomly distributed in the solid phase of the nano-silver paste. Therefore, a reasonable microstructural description is necessary to characterize the two-phase material.

Let  $(\Omega, \mathcal{F}, \mathbb{P})$  be a fixed probability space, where  $\Omega$  is a sample space,  $\mathcal{F}$  is a subset of the sample space, and  $\mathbb{P}$  is a function that assigns probabilities to events [40]. Let each point  $\omega \in \Omega$  denote a realization of the random porous materials within some subset  $V$  of  $D$ -dimensional Euclidean space, i.e.,  $V \in \mathbb{R}^D$ . The porous material is statistically described by a random variable  $\xi(\mathbf{x}, t; \omega)$ . The random variable  $\xi(\mathbf{x}, t; \omega)$  is a structure function which depends on position vectors  $\mathbf{x}$  of all points at the time  $t$  [41]. Assume the random micro-porous structure is approximately static and independent of time, the structure function can be taken as  $\xi(\mathbf{x}; \omega)$ . For two phase random micro-porous material, the space  $V \in \mathbb{R}^D$  is divided into solid phase region  $\mathcal{V}_0(\omega)$  and pore phase region  $\mathcal{V}_1(\omega)$ , where  $\mathcal{V}_0(\omega) \cup \mathcal{V}_1(\omega) = V$  and  $\mathcal{V}_0(\omega) \cap \mathcal{V}_1(\omega) = \emptyset$ . For a certain two-phase porous morphology, an indicator function  $\mathcal{I}(\mathbf{x}; \omega)$  can be derived from the structure function  $\xi(\mathbf{x}; \omega)$ , given for each position vectors  $\mathbf{x}$  by

$$\mathcal{I}(\mathbf{x}; \omega) = \begin{cases} 1, & \text{if } \mathbf{x} \in \mathcal{V}_1(\omega), \\ 0, & \text{if } \mathbf{x} \in \mathcal{V}_0(\omega). \end{cases} \quad (1)$$

For fixed position vector  $\mathbf{x}$ , the probability descriptions of solid phase region and pore phase region are given by  $\mathbb{P}\{\mathcal{I}(\mathbf{x}) = 0\}$  and  $\mathbb{P}\{\mathcal{I}(\mathbf{x}) = 1\}$ , which follows

$$\mathbb{P}\{\mathcal{I}(\mathbf{x}) = 0\} + \mathbb{P}\{\mathcal{I}(\mathbf{x}) = 1\} = 1. \quad (2)$$

Assume the micro-porous morphology is statistically homogeneous, the probability function  $S_1$  of an arbitrary point  $\mathbf{x}_1$  in the region  $V$ , also called one-point probability function, is given by

$$S_1(\mathbf{x}_1) = \mathbb{P}\{\mathcal{I}(\mathbf{x}_1) = 1\} = \phi_1, \quad (3)$$

where  $\phi_1$  is the volume fraction of pore phase. One-point probability function indicates the porosity of the nano-silver paste for each single point.

Assume the micro-porous material is isotropic, two-point probability function or autocorrelation functions  $S_2(\mathbf{x}_1, \mathbf{x}_2)$  is given by

$$S_2(\mathbf{x}_1, \mathbf{x}_2) = \mathbb{P}\{\mathcal{I}(\mathbf{x}_1) = 1, \mathcal{I}(\mathbf{x}_2) = 1\} = \begin{cases} \phi_1, & \text{if } |\mathbf{r}| = 0, \\ \phi_1^2, & \text{if } |\mathbf{r}| \rightarrow +\infty, \end{cases} \quad (4)$$

where random spatial vector  $\mathbf{r}$  is given by any two points  $\mathbf{x}_1, \mathbf{x}_2 \in V$

$$\mathbf{r} = \mathbf{x}_2 - \mathbf{x}_1. \quad (5)$$

Two-point function provides correlative information between each two points and involves the certain gross feature of the micro-porous structure [16]. This function can be used to examine the spatial similarity of the real and synthetic microstructures with the same porosity [21]. Hence, the suitable synthetic microstructure is determined by the two-point function.

## 2.2. One-cut Gaussian random field model

For numerical morphology generation, a Gaussian random field model with the vectors of random variables is given by

$$\mathbf{Z}(\omega) = [Z(\mathbf{x}_1, \omega), Z(\mathbf{x}_2, \omega), \dots, Z(\mathbf{x}_N, \omega)]^T, \quad \text{for any } \mathbf{x}_1, \mathbf{x}_2, \dots, \mathbf{x}_N \in V, \quad (6)$$

where  $Z(\mathbf{x}_1, \omega), \dots, Z(\mathbf{x}_N, \omega)$  are independent and identically follow the multivariate Gaussian distribution. That is,  $\mathbf{Z} \sim N(\boldsymbol{\mu}, C)$ , with the mean vector  $\boldsymbol{\mu} = [\mu_1, \mu_2, \dots, \mu_N]$  and the correlation matrix  $C = [c_{i,j}]$ , follows

$$\mu_i = \mu(\mathbf{x}_i) = \mathbb{E}(Z(\mathbf{x}_i)), \quad i = 1, \dots, N, \quad (7)$$

$$c_{ij} = Cov(\mathbf{x}_i, \mathbf{x}_j) = \mathbb{E}[(Z(\mathbf{x}_i) - \mu(\mathbf{x}_i))(Z(\mathbf{x}_j) - \mu(\mathbf{x}_j))], \quad i, j = 1, \dots, N. \quad (8)$$

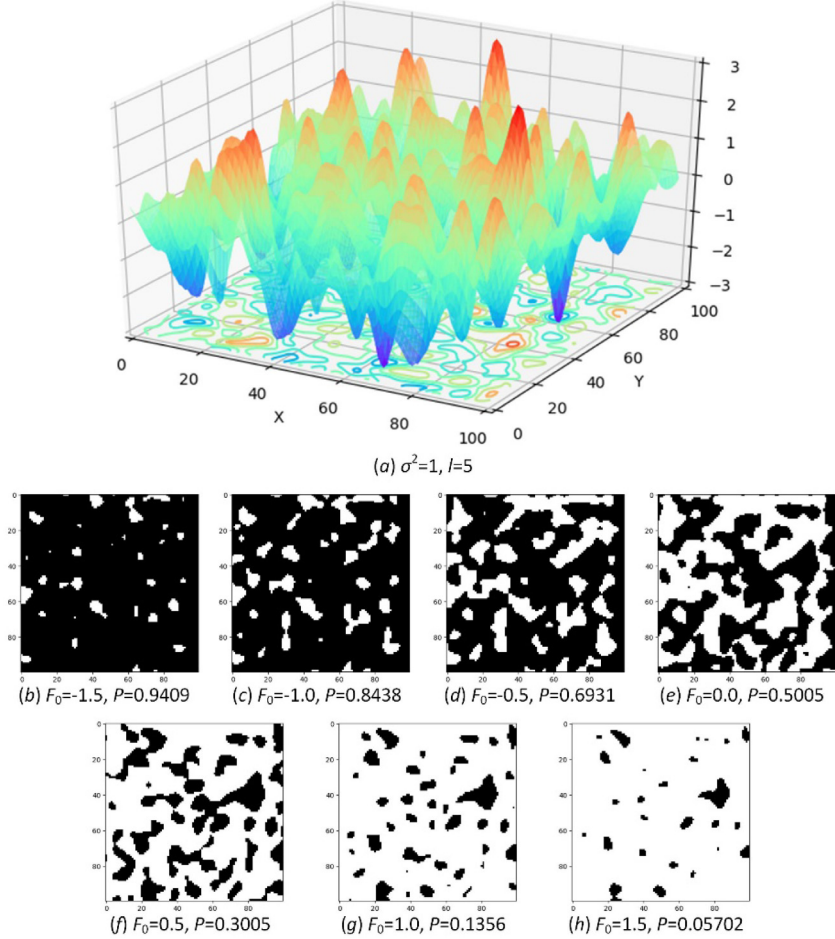


**Fig. 2.** One-cut Gaussian random field sample with different cut levels.

For simplicity, we consider the mean variable  $\mu_i = 0$  so that the mean vector  $\boldsymbol{\mu} = \mathbf{0}$  and  $\mathbf{Z} \sim N(\mathbf{0}, \mathbf{C})$ . Moreover, the Gaussian covariance function is given by [42]

$$Cov(\mathbf{x}_i, \mathbf{x}_j) = \sigma^2 \exp\left(-\frac{|\mathbf{x}_i - \mathbf{x}_j|^2}{l^2}\right), \quad l > 0 \text{ and } d \geq 1, \quad (9)$$

where  $\sigma$  is the variance of the two-point covariance value,  $l$  is the correlation length that influences the size of the neighbouring region, and  $d$  is the Euclidean dimension. Fig. 2(a) gives the three-dimensional random sample with  $\sigma^2 = 1$ ,  $l = 1$  by Gaussian random fields. Referring to [42], a cut level at a threshold value  $F_0$  is proposed to divide the random sample to pore phase region and solid phase region in the two-dimensional space. The indicator function  $\mathcal{I}$  can be defined as

$$\mathcal{I}(\mathbf{x}) = \begin{cases} 1, & \text{if } F(x) > F_0, \\ 0, & \text{if } F(x) < F_0. \end{cases} \quad (10)$$

The cut level  $F_0$  is a significant contributory factor to the area fraction of pore phase in the synthetic microstructure. Fig. 2(b)–(h) show the gradual decrease in the porosity  $P$  for microstructure samples with the increasing cut level  $F_0$ . We can use cut level  $F_0$  to control the porosity  $P$  at the target value.

The relationships between the cut level  $F_0$  and the porosity  $P$  are further investigated with different correlation length  $l$  and variance  $\sigma$  of the Gaussian covariance function, as shown in Fig. 3(a)–(c). It can be seen that the porosity

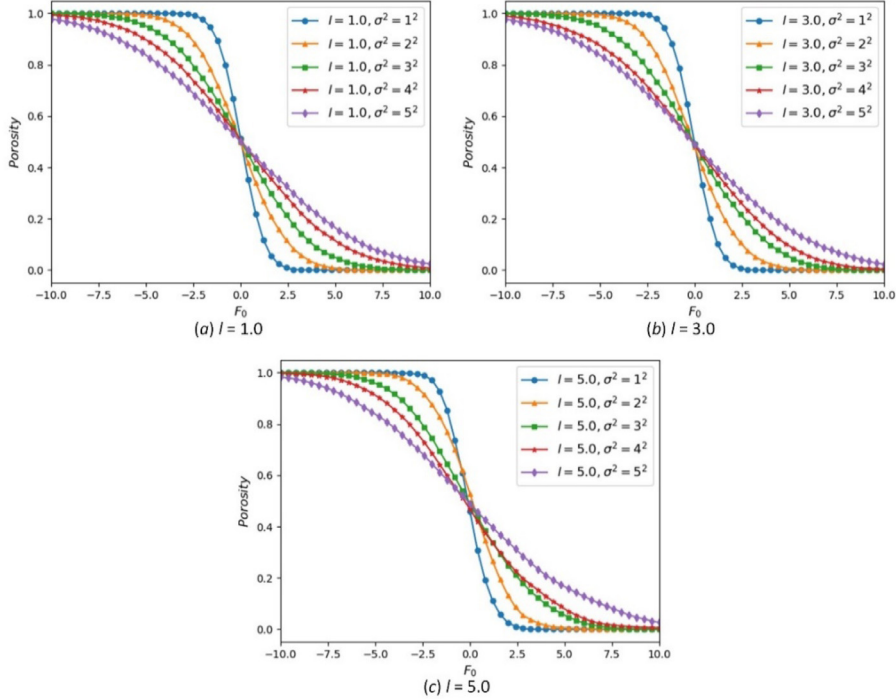


**Fig. 3.** The relationships between the cut level  $F_0$  and the porosity  $P$  with different correlation length  $l$  and variance  $\sigma$ .

$P$  starts from 1.0 and approaches 0.0 with increasing  $F_0$ , and the porosity  $P$  is nearly equal to 0.5 when  $F_0$  is 0.0. Variance  $\sigma$  appears to affect the descent rate and range of the porosity curves, where the descent rate decreases and the descent range increases with the increasing value of variance  $\sigma$ . However, no significant differences are found between different correlation length  $l$  with the same variance. For a stable cut level and controllable morphology generation, the variance  $\sigma$  is set to 1.0.

For a given  $100 \times 100$  square region, the correlation length  $l$ , ranging from 1.0 to 5.0, with fixed variance and porosity ( $\sigma = 1.0$ ,  $P = 0.2$ ) is used to generate Gaussian random field samples and obtain varied two-dimensional morphologies, as shown in Fig. 4(a)–(d). Comparing with the five random morphologies in Fig. 4, the correlation length  $l$  can represent the feature size of each single pore, where the average pore size increases with the increasing correlation length  $l$ . In other words, the number of pores, in the region of the same size and porosity, declines when the correlation length  $l$  increases. By adjusting the region size and correlation length, we can obtain more detailed information and generate more accurate sampling results to be close to the real nano-silver sintering morphology of a fixed porosity.

### 2.3. Random morphology generation and verification

Random micro-porous morphology, generated by Gaussian random field model, is a two-phase material with specific spatial characteristics. The spatial distribution characteristics of the micro-porous morphology are extracted from the microstructure to verify the similarity between the real and synthetic ones. The spatial characteristics are a partial information of the two-phase topological distribution, which can be used to describe the overall microstructural property of the microporous morphology. Referring to [41], two-point probability function is an effective approach to obtain the spatial characteristics from a two-phase topology, providing the information on certain gross microstructural features as well as the similarity between different micro-porous morphologies. In this paper, the two-point probability function  $S_2(\mathbf{x}_1, \mathbf{x}_2)$ , given by Eq. (4), is used to analyse the spatial correlations between the pore-phase points and determine whether the generated morphology is able to represent the observed microstructure.

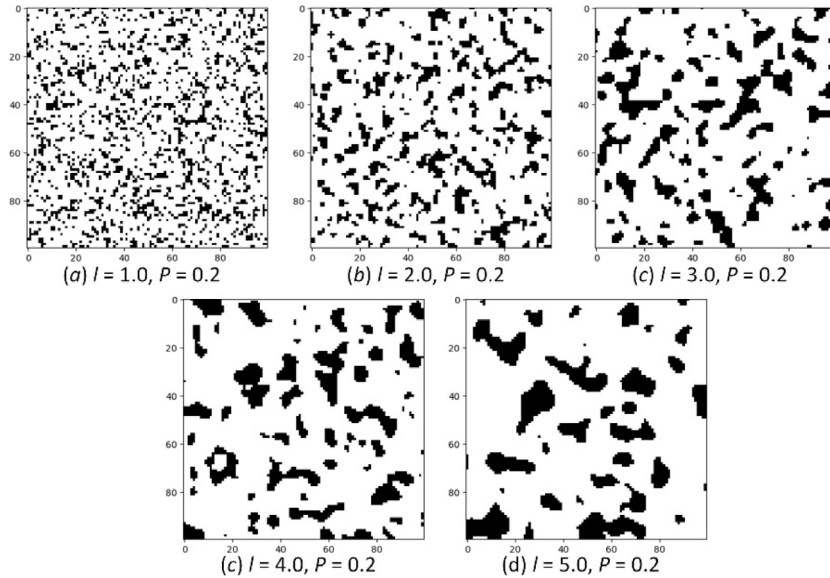


**Fig. 4.** Random morphologies with different correlation length  $l$  in the region of  $100 \times 100$ .

To examine the two-point probability function  $S_2$ , different correlation length  $l$ , ranging from 1.0 to 5.0, and porosity  $P$ , ranging from 0.05 to 0.20, are chosen to generate two-dimensional micro-porous morphologies. The two-point probability function  $S_2$  for the pore phase in these morphologies is shown in Fig. 5(a)–(d). In Fig. 5(a)–(d), the  $S_2$  values of the different  $l$  are all starting from 0.05 and ending with 0.0025, where the starting point is equal to  $P$  and the end point is approximately  $P^2$ . Thus, the  $S_2$  curves have a good discrimination capability for the morphologies of different porosity. Moreover, another finding is that the  $S_2$  curves are sensitive to the feature sizes of the pores in the morphologies with variant correlation length  $l$ . When the correlation length  $l$  is smaller, the decrease rate of the curve is higher and the two-point distance  $r$  at the first minimum point is smaller. Here, we choose the decrease rate to characterize the same pore feature size of the morphology. To summarize, two-point probability function  $S_2$  can be employed to quantify the differences between real microstructure and random morphology, and select the most realistic random micro-porous morphologies for further simulations.

Based on above function, Area 1, Area 2, and Area 3 in Fig. 1, which have a porosity of 0.2259, 0.1098 and 0.1556 respectively, are considered as the most realistic morphologies and selected to generate the synthetic ones. The size and porosity of the real and synthetic morphologies are compared in Table 1. The sample area is  $10 \times 10 \mu\text{m}^2$ , and the pixel size is  $0.05 \mu\text{m}$ . Thus, the sample size of the random synthetic morphologies, S1-GRF, S2-GRF and S3-GRF, is  $200 \times 200$  pixels. During Gaussian random field sampling, the cut levels of S1-GRF, S2-GRF, and S3-GRF can be adjusted to obtain the porosities consistent with Area 1, Area 2, and Area 3, respectively. Further, we can control the correlation length  $l$  to adjust the pore feature size of the samples and align with the real morphology.

The two-point probability function is developed to verify the consistency of properties between real and synthetic morphologies, as shown in Fig. 6(a). The random morphologies, which are generated by Gaussian random field model and verified by the two-point probability function, are shown in Fig. 6(b)–(d). Comparing to the real microstructures shown in Fig. 1, the gross features of synthetic morphologies demonstrate good agreements. It also can be found that the porosities of the real and synthetic ones are the same and the deviations of decrease rates are within 5%, which prove the similarities of the pore feature size between the real and synthetic morphologies.

The images of real morphologies, obtained by experimental methods, are limited in quantities due to the high costs associated with acquiring them. It is difficult to adequately represent the random porous materials with a limited number of real morphologies. However, using the one-cut Gaussian random field model, random micro-porous morphologies could be generated without quantitative limitations. The generated images of morphologies, with similar spatial features to the real morphologies, could be utilized to analyse the statistical properties of the

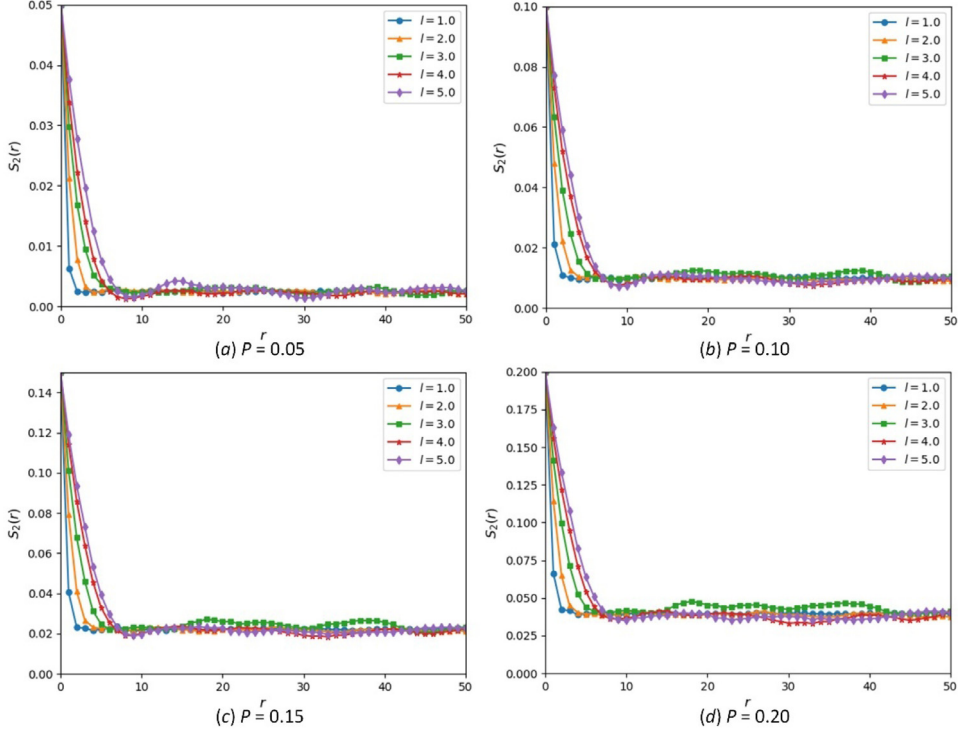


**Fig. 5.** Two-point probability functions of different correlation lengths and porosities.

**Table 1**  
The size and porosity of the real and synthetic morphologies.

Sample	Area size ( $\mu\text{m}^2$ )	Porosity	Pixel size ( $\mu\text{m}$ )
Area 1	$10 \times 10$	0.2259	0.05
Area 2	$10 \times 10$	0.1098	0.05
Area 3	$10 \times 10$	0.1556	0.05
S1-GRF	$10 \times 10$	0.2259	0.05
S2-GRF	$10 \times 10$	0.1098	0.05
S3-GRF	$10 \times 10$	0.1556	0.05

material behaviours. Therefore, many random micro-porous morphologies are produced by the one-cut Gaussian random field model in this paper.

### 3. Phase field model for thermo-elasto-plastic body

#### 3.1. Primary fields and state variables

Consider an arbitrary domain  $\Omega \subset \mathbb{R}^D$  describing the deformation, temperature and phase fields of a thermo-elasto-plastic body with internal crack  $\Gamma$  and external boundary  $\partial\Omega \subset \mathbb{R}^{D-1}$  over time period  $\mathcal{T} = [0, t_a]$ , as shown in Fig. 7. The state of this domain is defined by introducing five independent state variables, including traction variable  $t(\mathbf{x})$ , displacement variable  $\mathbf{u}(\mathbf{x})$ , heat flux variable  $\mathbf{q}(\mathbf{x})$ , temperature variable  $\theta(\mathbf{x})$  and phase field variable  $d(\mathbf{x})$ . Here, the phase-field variable represents the damage status where  $d = 0$  for undamaged material and  $d = 1$  for broken material.

The internal crack  $\Gamma$  with a regularized crack topology in the whole body is defined as the volume integral of the crack surface density  $\gamma(d, \nabla d)$ , given by [43,44],

$$\Gamma = \int_{\Omega} \gamma(d, \nabla d) \, d\Omega = \frac{1}{2l_c} \int_{\Omega} (d^2 + l_c^2 |\nabla d|^2) \, d\Omega, \quad (11)$$

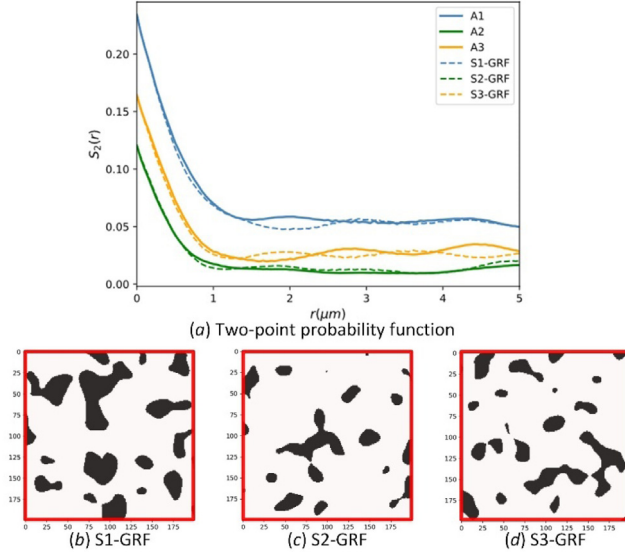


**Fig. 6.** The two-point probability functions of the real and synthetic morphologies.

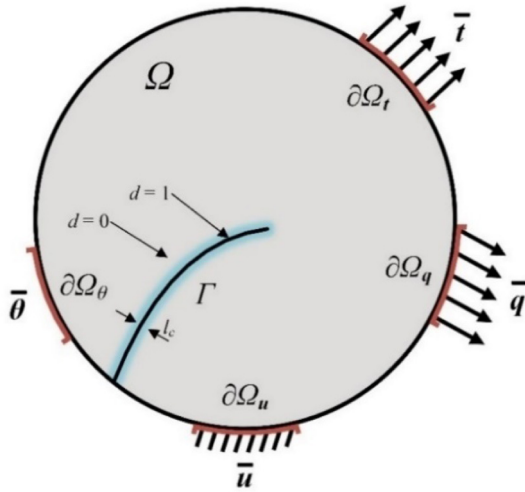


**Fig. 7.** Deformed configuration of the thermo-elasto-plastic solids body with a smeared crack.

where  $l_c$  is a length-scale parameter to govern the size of diffusive zone. The whole external boundary  $\partial\Omega$  is composed of four boundaries including the traction boundary  $\partial\Omega_t$ , the displacement boundary  $\partial\Omega_u$ , the heat flux boundary  $\partial\Omega_q$  and the temperature boundary  $\partial\Omega_\theta$ , where  $\partial\Omega_t \cap \partial\Omega_u = \emptyset$ ,  $\partial\Omega_t \cup \partial\Omega_u = \partial\Omega$  and  $\partial\Omega_q \cap \partial\Omega_\theta = \emptyset$ ,  $\partial\Omega_q \cup \partial\Omega_\theta = \partial\Omega$ . The boundary conditions of traction  $t(x)$ , displacement  $u(x)$ , heat flux  $q(x)$ , and temperature  $\theta(x)$  are prescribed as:

$$\begin{aligned} \bar{t}: \partial\Omega_t \times \mathcal{T} &\rightarrow \mathbb{R}^D, & \bar{u}: \partial\Omega_u \times \mathcal{T} &\rightarrow \mathbb{R}^D, \\ \bar{q}: \partial\Omega_q \times \mathcal{T} &\rightarrow \mathbb{R}^1, & \bar{\theta}: \partial\Omega_\theta \times \mathcal{T} &\rightarrow \mathbb{R}^1. \end{aligned} \quad (12)$$

The multi-field setting of state variables in thermo-elasto-plastic body is defined by five independent variables, shown as

$$S := \{t, u, q, \theta, d\}, \quad (13)$$

where

$$\begin{aligned} \boldsymbol{t}: \Omega_t \times \mathcal{T} &\rightarrow \mathbb{R}^D, & \boldsymbol{u}: \Omega_u \times \mathcal{T} &\rightarrow \mathbb{R}^D, \\ \boldsymbol{q}: \Omega_q \times \mathcal{T} &\rightarrow \mathbb{R}^1, & \theta: \Omega_\theta \times \mathcal{T} &\rightarrow \mathbb{R}^1. \end{aligned} \quad (14)$$

In this paper, the proposed complex multi-field model involves three main processes, including thermal process, mechanical process, and fracture process. Among these processes, the multi-field interactions in the thermo-elasto-plastic body are investigated, which include interactions between temperature and elasticity/plasticity as well as between phase-field fracture and thermo-elasto-plastic response.

### 3.2. Energy functional

The total energy density functional of the thermo-elasto-plastic body is defined as

$$\psi(\boldsymbol{u}, \theta, d) = \psi^e(\boldsymbol{u}, \theta, d) + \psi^p(\boldsymbol{u}, \theta, d) + \psi^\theta(\theta, d) + \psi^d(d), \quad (15)$$

where  $\psi^e$  is the elastic strain energy density,  $\psi^p$  is the plastic strain energy density,  $\psi^\theta$  is the purely thermal contribution to the energy, and  $\psi^d$  is the phase-field fracture energy density. It shows the coupling of the temperature field and deformation field in the solid.

Based on Ref. [43], the elastic strain energy density with isotropic degradation is given by

$$\psi^e(\boldsymbol{u}, \theta, d) = g(d) \psi_0^e(\boldsymbol{u}, \theta), \quad (16)$$

where  $g(d)$  is the degradation function and  $\psi_0^e$  is the elastic energy density of an undamaged solid. According to Ref. [43], the degradation function follows a squarish form

$$g(d) = (1 - d)^2 + \zeta, \quad (17)$$

where  $\zeta$  is a small number for computing stability (on the order of  $10^{-8}$ ). The elastic energy density  $\psi_0^e$  without damage is defined as

$$\psi_0^e(\boldsymbol{u}, \theta) = \frac{\lambda(\theta)}{2} \text{tr}^2[\boldsymbol{\epsilon}^e(\boldsymbol{u})] + \mu(\theta) \text{tr}[\boldsymbol{\epsilon}^{e2}(\boldsymbol{u})] \quad (18)$$

where  $\lambda(\theta)$  and  $\mu(\theta)$  are two elastic moduli dependent on temperature  $\theta$ . Here, we assume the variation of the Poisson's ratio  $\nu$  with temperature is negligible [45,46] while the Young's modulus at various temperatures can be described as

$$E(\theta) = E_0 - B\theta \exp(-\theta_0/\theta) \quad (19)$$

where  $E_0$  is the Young's modulus at a reference temperature  $\theta_0$ , and  $B$  is an empirical coefficient. Based on above assumptions, the Lamé's first parameter  $\lambda(\theta)$  and shear modulus  $\mu(\theta)$  are derived as:

$$\lambda(\theta) = \frac{\nu [E_0 - B\theta \exp(-\theta_0/\theta)]}{(1 + \nu)(1 - 2\nu)}, \quad (20)$$

$$\mu(\theta) = \frac{E_0 - B\theta \exp(-\theta_0/\theta)}{2(1 + \nu)}. \quad (21)$$

According to Refs. [22,47], the plastic energy density function can be expressed as

$$\psi^p(\boldsymbol{u}, \theta, d) = g(d) \psi_0^p(\boldsymbol{u}, \theta). \quad (22)$$

Considering the von Mises yield criterion [48] influenced by the temperature, the yield function is defined as

$$f(\boldsymbol{\sigma}) = \sigma_{eq} - g(d) [\sigma^{lim}(\theta) + H(\theta) \varepsilon_{eq}^p], \quad (23)$$

where  $\sigma_{eq}$  is the von Mises stress,  $\varepsilon_{eq}^p$  is the energy equivalent plastic shear strain,  $\sigma^{lim}(\theta)$  is the initial yield strength, and  $H(\theta)$  is the hardening modulus. To describe this inelastic response with temperature, the initial yield strength  $\sigma^{lim}(\theta)$  and the hardening modulus  $H(\theta)$  are defined as [49],

$$\sigma^{lim}(\theta) = \omega_1 \exp\left(\frac{\omega_2}{\theta}\right) \quad (24)$$

$$H(\theta) = \omega_3 \exp\left(\frac{\omega_4}{\theta}\right) \quad (25)$$

where  $\omega_1$ ,  $\omega_2$ ,  $\omega_3$ , and  $\omega_4$  are the yield parameters fitted from the experimental data. Assume there is no damage in the solid, the plastic part of the energy history is given by

$$\psi_0^p(\mathbf{u}, \theta) = \varepsilon_{eq}^p(\mathbf{u}) \left[ \sigma^{lim}(\theta) + \frac{1}{2} H(\theta) \varepsilon_{eq}^p(\mathbf{u}) \right]. \quad (26)$$

In this paper, the total strain  $\boldsymbol{\varepsilon}$  is divided into three parts, including elastic ( $\boldsymbol{\varepsilon}^e$ ), plastic ( $\boldsymbol{\varepsilon}^p$ ), and thermal expansion  $\boldsymbol{\varepsilon}^\theta$  parts. For small-strain plasticity, the elastic and plastic strains are given by

$$\boldsymbol{\varepsilon}^e + \boldsymbol{\varepsilon}^p = \boldsymbol{\varepsilon} - \boldsymbol{\varepsilon}^\theta. \quad (27)$$

The total strain  $\boldsymbol{\varepsilon}$  is defined by the deformation gradient as:

$$\boldsymbol{\varepsilon} = \frac{1}{2} (\nabla \mathbf{u} + \nabla \mathbf{u}^T), \quad (28)$$

and the thermal expansion strain  $\boldsymbol{\varepsilon}^\theta$  is defined as:

$$\boldsymbol{\varepsilon}^\theta = \alpha_\theta \Delta \theta \mathbf{I}, \quad (29)$$

where  $\alpha_\theta$  is the thermal expansion coefficient and  $\mathbf{I}$  is the identity tensor.

Based on Refs. [25,26], the purely thermal contribution to the total energy functional is assumed as,

$$\psi^\theta(\theta) = c \left( \theta - \theta_a - \theta \ln \left( \frac{\theta}{\theta_a} \right) \right), \quad (30)$$

where  $c \geq 0$  is the specific heat capacity and  $\theta_a$  is the initial temperature. Assume the heat conduction to be governed by Fourier law, the heat flux  $\mathbf{q}$  follows the form as

$$\mathbf{q}(\mathbf{u}, d, \theta) = -g(d) \mathbf{k}(\mathbf{u}, \theta) \nabla \theta, \quad (31)$$

where  $\mathbf{k}(\mathbf{u}, \theta)$  is the material conductivity tensor.

Considering the smeared fracture phase-field, the fracture energy can be approximated as:

$$\int_{\Gamma} g_c d\Gamma = \int_{\Omega} \frac{g_c}{2l_c} (d^2 + l_c^2 |\nabla d|^2) d\Omega \quad (32)$$

where  $g_c$  is the surface energy for a unit fracture surface. Thus, the phase-field fracture energy density can be expressed as:

$$\psi^d = \frac{g_c}{2l_c} (l_c^2 \nabla d \cdot \nabla d + d^2). \quad (33)$$

Based on above energy density functional, the Lagrangian function  $L$  for this thermo-elasto-plastic problem is given as

$$\begin{aligned} L(\mathbf{u}, \dot{\mathbf{u}}, \theta, d) &= \int_{\Omega} \left( \frac{1}{2} \rho \dot{\mathbf{u}} \cdot \dot{\mathbf{u}} + \mathbf{b} \cdot \mathbf{u} + \rho c \dot{\theta} + \nabla \cdot \mathbf{q} - S - \psi^e(\mathbf{u}, \theta, d) - \psi^p(\mathbf{u}, \theta, d) - \psi^\theta(\theta, d) \right) dV \\ &\quad + \int_{\partial \Omega_t} \bar{\mathbf{t}} \cdot \mathbf{u} dA + \int_{\partial \Omega_q} \bar{\mathbf{q}} \cdot \mathbf{u} dA - \int_{\Omega} \frac{g_c}{2l_c} (d^2 + l_c^2 |\nabla d|^2) dV, \end{aligned} \quad (34)$$

where  $\rho$  is the material density,  $\mathbf{b}$  is the force per unit mass of the body, and  $S$  is the heat source per unit volume of the body.

### 3.3. Governing equations

The governing equations for this coupled thermo-elasto-plastic problem are summarized in Table 2. In this phase-field framework, the mathematics models of the Dirichlet and Neumann boundary conditions derived from the Lagrangian function can be classified into three groups: (a) deformation-related equations, (b) temperature-related

**Table 2**

Governing equations in the thermo-elasto-plastic solids.

Deformation-related equations	$\text{div}\sigma + \mathbf{b} = \rho\ddot{\mathbf{u}}$	in $\Omega \times \mathcal{T}$	(35)
	$\sigma \cdot \mathbf{n} = \bar{\mathbf{t}}$	on $\partial\Omega_t \times \mathcal{T}$	(36)
	$\mathbf{u} = \bar{\mathbf{u}}$	on $\partial\Omega_u \times \mathcal{T}$	(37)
Temperature-related equations	$\rho c\dot{\theta} + \nabla \cdot \mathbf{q} = S$	in $\Omega \times \mathcal{T}$	(38)
	$\mathbf{q} \cdot \mathbf{n} = \bar{\mathbf{q}}$	on $\partial\Omega_q \times \mathcal{T}$	(39)
	$\theta = \bar{\theta}$	on $\partial\Omega_\theta \times \mathcal{T}$	(40)
Damage-related equations	$2(1-d)(\psi^e + \psi^p + \psi^\theta) - \frac{g_c}{l_c}(d - l_c^2 \nabla d) = 0$	in $\Omega \times \mathcal{T}$	(41)
	$\nabla d \cdot \mathbf{n} = 0$	on $\partial\Omega \times \mathcal{T}$	(42)

equations, (c) damage-related equations. Here, Eq. (35) shows the local conservation of momentum with the Cauchy stress  $\sigma$ , Eqs. (36) and (37) are Neumann boundary conditions for deformation with the outward normal  $\mathbf{n}$ . Eq. (38) describes the temperature evolution of the thermal equilibrium, Eqs. (39) and (40) are thermal boundary conditions. Eq. (41) expresses the crack phase-field evolution by damage, Eq. (42) is boundary conditions for damage.

Further, considering the irreversibility of the damage, the history energy variable  $\mathcal{H}(\mathbf{u}, \theta, d)$  is defined as

$$\mathcal{H}(\mathbf{u}, \theta, d) = \max_{\tau \in [0, t]} [\psi^e(\mathbf{u}, \theta, d) + \psi^p(\mathbf{u}, \theta, d) + \psi^\theta(\theta, d)]. \quad (43)$$

Thus, the thermo-elasto-plastic energy density functions in Eq. (41) are replaced by history energy variable  $\mathcal{H}$ . The governing equation for this phase field problem can be given as

$$2(1-d)\mathcal{H} - \frac{g_c}{l_c}(d - l_c^2 \nabla d) = 0. \quad (44)$$

### 3.4. Spatial and temporal discretization

To realize the phase-field method and solve the thermo-elasto-plastic coupling problem, a spatial and temporal discretization scheme is developed to discretize the governing equations and implement the phase-field method in Abaqus using user-defined subroutines.

The displacement  $\mathbf{u}$ , temperature  $\theta$ , and damage  $d$  of a mixed finite element are discretized in space and time. The spatial-discrete element with the first-order shape function at time  $t$  can be approximated as

$$\mathbf{u}(\mathbf{x}, t) = \sum_{i=1}^{N_{node}} N_i^u(\mathbf{x}) \mathbf{u}_i(t), \quad \theta(\mathbf{x}, t) = \sum_{i=1}^{N_{node}} N_i^\theta(\mathbf{x}) \theta_i(t), \quad d(\mathbf{x}, t) = \sum_{i=1}^{N_{node}} N_i^d(\mathbf{x}) d_i(t), \quad (45)$$

where  $N_i^u(\mathbf{x})$ ,  $N_i^\theta(\mathbf{x})$  and  $N_i^d(\mathbf{x})$  are the node  $i$ th shape functions [50],  $\mathbf{u}_i(t)$ ,  $\theta_i(t)$  and  $d_i(t)$  represent the node  $i$ th displacement, temperature and damage variables at time  $t$ .  $N_{node}$  is the number of the nodes in one element. Then, the derivatives of displacement, temperature and damage are respectively given by

$$\boldsymbol{\varepsilon}(\mathbf{x}, t) = \sum_{i=1}^{N_{node}} B_i^u(\mathbf{x}) \mathbf{u}_i(t), \quad \nabla\theta(\mathbf{x}, t) = \sum_{i=1}^{N_{node}} B_i^\theta(\mathbf{x}) \theta_i(t), \quad \nabla d(\mathbf{x}, t) = \sum_{i=1}^{N_{node}} B_i^d(\mathbf{x}) d_i(t), \quad (46)$$

where  $B_i^u(\mathbf{x})$ ,  $B_i^\theta(\mathbf{x})$  and  $B_i^d(\mathbf{x})$  stand for the derivative matrices of the shape functions.

The residual vectors for displacement, temperature and damage are considered as

$$\begin{aligned} \mathbf{r}_i^u &= \int_{\Omega} g(d) (B_i^u)^T \sigma dV - \int_{\Omega} (N_i^u)^T \mathbf{b} dV - \int_{\partial\Omega_t} (N_i^u)^T \bar{\mathbf{t}} dA, \\ r_i^\theta &= \int_{\Omega} g(d) (B_i^\theta)^T B_i^\theta \theta dV - \int_{\Omega} (N_i^\theta)^T S dV - \int_{\Omega} (N_i^\theta)^T \bar{\mathbf{q}} dA, \\ r_i^d &= \int_{\Omega} \left\{ g_c l_c (B_i^d)^T \nabla d - \left[ 2(1-d)\mathcal{H} - \frac{g_c}{l_c} d \right] N_i^d \right\} dV. \end{aligned} \quad (47)$$

The equation system of the coupled problem is nonlinear, and should be discretized in time. For temporal discretization, the total time interval  $[0, t_a]$  could be divided into several small intervals:  $0 = t_0 < t_1 < \dots < t_n <$

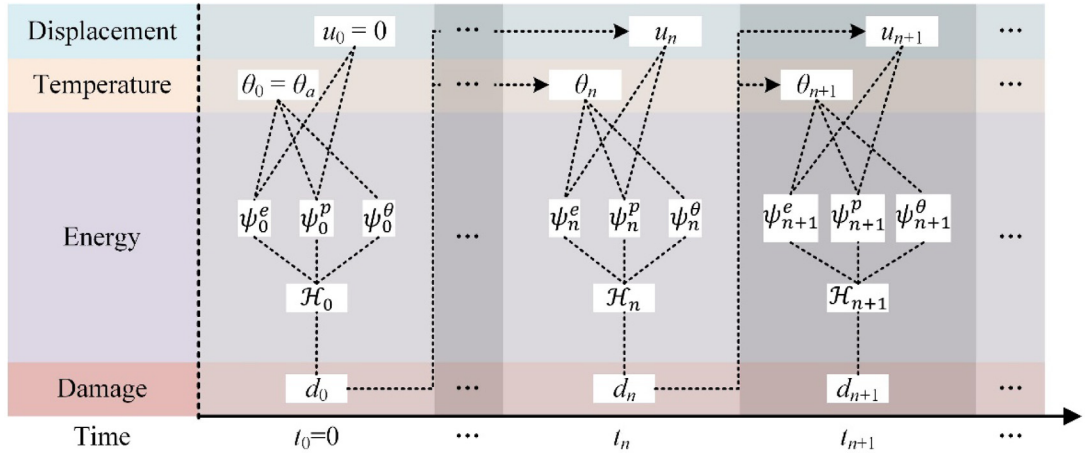


**Fig. 8.** Flowchart of the incremental solution utilized to solve the displacement–temperature–phase-field problems.

$t_{n+1} < \dots < t_N = t_a$ . Consider a finite time increment  $[t_n, t_{n+1}]$ , an incremental calculation scheme is implemented to decouple the displacement field, temperature field, and phase field. With a Newton–Raphson nonlinear solver, the corresponding iteration could be obtained as

$$\begin{Bmatrix} \mathbf{u} \\ \theta \\ d \end{Bmatrix}_{n+1} = \begin{Bmatrix} \mathbf{u} \\ \theta \\ d \end{Bmatrix}_n - \begin{bmatrix} \mathbf{K}^{uu} & 0 & 0 \\ 0 & \mathbf{K}^{\theta\theta} & 0 \\ 0 & 0 & \mathbf{K}^{dd} \end{bmatrix}^{-1} \begin{Bmatrix} \mathbf{r}^u \\ \mathbf{r}^\theta \\ \mathbf{r}^d \end{Bmatrix}_n, \quad (48)$$

where

$$\begin{aligned} \mathbf{K}_{ij}^{uu} &= \frac{\partial \mathbf{r}_i^u}{\partial \mathbf{u}_j} = \int_{\Omega} g(d) (\mathbf{B}_i^u)^T \mathbf{E}^{epc} \mathbf{B}_j^u dV, \\ \mathbf{K}_{ij}^{\theta\theta} &= \frac{\partial \mathbf{r}_i^\theta}{\partial \theta_j} = \int_{\Omega} g(d) (\mathbf{B}_i^\theta)^T \mathbf{K} \mathbf{B}_i^\theta \mathbf{B}_j^\theta dV, \\ \mathbf{K}_{ij}^{dd} &= \frac{\partial \mathbf{r}_i^d}{\partial d_j} = \int_{\Omega} \left[ g_{clc} (\mathbf{B}_i^d)^T \mathbf{B}_j^d + \left( 2\mathcal{H} + \frac{g_c}{l_c} \right) N_i^d N_j^d \right] dV. \end{aligned} \quad (49)$$

where  $\mathbf{E}^{epc}$  is the consistent Jacobian matrix,  $\mathbf{K}$  is the heat transfer coefficient matrix.

A flowchart of a time-increment numerical method was proposed to decouple and solve this thermo-elasto-plastic problem, as shown in Fig. 8. To begin this solution, the displacement  $u_0$  and temperature  $\theta_0$  are initialized, where  $u_0 = 0$  and  $\theta_0 = \theta_a$ . Based on this initialization, elastic strain energy  $\psi_0^e$ , plastic strain energy  $\psi_0^p$ , and purely thermal contribution  $\psi_0^\theta$  are obtained. Here, both displacement and temperature influence elastic and plastic strain energies, while thermal energy  $\psi_0^\theta$  is purely affected by temperature. Based on the above energies, the initial history energy  $\mathcal{H}_0$  and the initial damage value  $d_0$  can be calculated.

Then, the iterative computing scheme for each time increment is adopted to obtain the values of the displacement, temperature, energy and damage at a time point. At time  $t_n$ , this staggered scheme utilizes the displacement  $u_n$  and temperature  $\theta_n$  to compute the history energy  $\mathcal{H}_n$ . Further, the damage  $d_n$  could also be computed to describe the damaged material at time  $t_n$ . Subsequently, the displacement  $u_{n+1}$  and temperature  $\theta_{n+1}$  for the damaged body (indicated by  $d_n$ ) are updated from  $t_n$  to  $t_{n+1}$ . Based on the iteration above, all variables of the damaged body at a certain time point could be obtained.

#### 4. Numerical scheme and implementation

In this section, a new approach for phase field simulation of thermo-elasto-plastic porous material was proposed, as shown in Fig. 9. This approach could be divided into two parts, where the first part is microstructure-based random morphology generation and the second part is phase field simulation for mechanical and fracture behaviours.

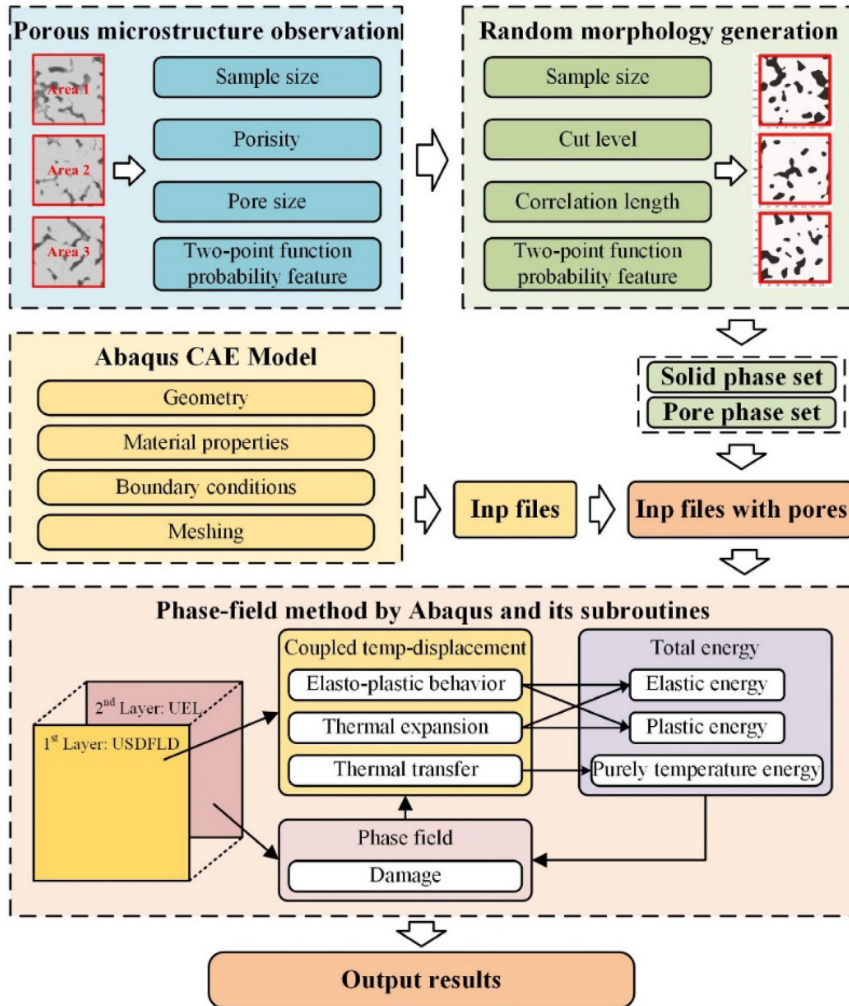


**Fig. 9.** The scheme of phase field simulation of thermo-elasto-plastic porous solids.

Based on the gaussian random fields, plenteous random porous morphologies are generated to represent the real microstructures. Further, phase field simulations of the generated morphologies are carried out to analyse the stress-strain responses and fracture evolutions, which could describe the mechanical behaviours of random porous microstructures thoroughly and statistically.

Microstructure-based random porous morphology could be obtained via two steps: microscopy imaging and random morphology generation. By microscopy imaging, the spatial features of the porous microstructures are extracted and analysed. Based on the observed microstructural grey-scale images, binary images with the solid-pore information could be obtained by setting a certain threshold. Then, the spatial features of the binary images, including sample size, porosity, and pore size, are analysed and determined. Further, the two-point probability function of the solid-pore microstructures could be calculated and plotted. Utilizing the one-cut gaussian random field model, the random micro-porous morphologies could be generated with the model parameters of target sample size, cut-level, and correlative length. Comparing the two-point probability functions of the experimental microstructure and the random morphologies, the similar and realistic synthetic morphologies are eventually finalized. Based on this, both solid and pore phase sets of the random micro-porous morphologies could be obtained to support the construction of the finite element (FE) models for porous materials.

In this method, Abaqus CAE is utilized to construct geometric model, set material properties, apply boundary conditions and mesh the model. The input file of the model without pores could be exported by Abaqus CAE.

Considering the solid-pore information, solid phase sets and pore phase sets could be added to the input file by python script. The processed input file with the porous microstructure includes two-layer elements, where the first layer elements are the built-in coupled temperature–displacement elements, and the second layer elements are the UEL phase field elements.

The phase field simulation is realized by Abaqus and its use-defined subroutines. The subroutines USDFLD and UEL are used in a two-layer approach. In the first layer, Abaqus and its subroutine USDFLD are utilized to solve the coupled temperature–displacement problems by the built-in solver. Then, USDFLD could access the material point data, such as the displacement, temperature, and corresponding energies, and update the solution-dependent state variables and field valubles to control the influence of damage on the material properties. In the second layer, the subroutine UEL utilizes the history energy to compute the damages to the material points. The phase field value could also be obtained and delivered to the first layer. This iterative process drives the material properties degradations and phase field evolutions. As the results of this approach, the stress–strain responses and phase field values of the thermo-elasto-plastic solids could be outputted, giving the mechanical and fracture behaviours of the porous material.

## 5. Numerical experiments and discussions

In this section, several numerical examples were carried out to validate the proposed approach for randomly distributed micro-porous sintered nano-silver structures, including:

- One element: uniaxial tensile tests under different temperature. This benchmark numerical example is conducted to verify the material properties and stress–strain responses for the single solid-phase material element under specific temperature conditions.
- Random porous microstructures: mechanical behaviours and fracture evolutions. Based on the observed microstructures, several examples of random micro-porous morphologies with some specific porosities are simulated to investigate the mechanical behaviours and fracture evolutions influenced by the random spatial structures, which also are compared with the experimental data to validate the proposed model and its effectiveness.
- Nano-silver sintering structure: thermal cyclic conditions and crack networks analysis. A more complex example aims to demonstrate the fracture evolutions and crack networks in the sintered nano-silver under thermal cyclic conditions. The features of the crack networks in both experimental and numerical results are compared and analysed.

### 5.1. One element: uniaxial tensile tests under different temperature

The examples of the one element are carried out to understand this phase field model of thermo-elasto-plastic solids. For the one element, the uniaxial tensile tests, as benchmark tests, under some specific temperatures are implemented to a 2D single solid-phase element. The geometry parameters and boundary conditions are shown in Fig. 10.

The size of the element is  $0.0002 \times 0.0002$  mm, which is related to the pixel size of the generated morphologies. The temperature value  $\theta$  is separately given as 233.0 K, 298.0 K, and 523.0 K. The displacement  $u(t) = 0.05t$  mm. Additionally, the total time is 1.00, and the step time increment is 0.0004. Referring to [16,51,52], the material properties of nano-silver micro-porous paste, including the solid- and pore/fracture-phase parameters, are given in Table 3. Considering the definition of the degradation function and the stability of the iterative computations, an approximately small value is adopted for pore/fracture phase. The fracture length scale  $l_c$  is 0.0004 mm, which satisfy the required relationships between  $l_c$  and mesh size according to Ref. [44].

The results of this benchmark example are obtained using the proposed model and adjust, shown in Fig. 11. Based on the numerical results of the silver element at room temperature, the elastic modulus is  $8.06 \times 10^5$  MPa, the UTS is 299.147 MPa, and the strain to failure is 0.036. The results are in a good agreement with the experimental data at room temperature, where the elastic modulus is  $8.15 \times 10^5$  MPa, the UTS is 300.0 MPa, and the strain to failure is 0.035. Besides, the numerical example shows the effect of temperature on mechanical response, that is, both elastic modulus and UTS decrease with increases of temperature, while the strain to failure increases. Additionally, this one element model shows more brittleness at low temperature, and more ductility at high temperature. Using this one element model as a benchmark, we carry out the subsequent simulations.

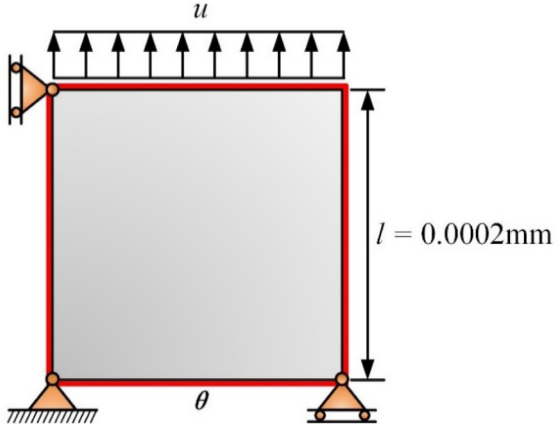


**Fig. 10.** Geometry parameters and boundary conditions for the uniaxial tensile test of one element.

**Table 3**

Material setting of the nano-silver micro-porous structures used for the numerical experiments [16,44,51,52].

Elastic parameters				
Young's modulus	$E_0$	81 500.00 $8.15 \times 10^{-4}$	(MPa) (MPa)	Solid phase Pore/Fracture phase
Poisson's ratio	$\nu$	0.38 0.38	(1) (1)	Solid phase Pore/Fracture phase
Empirical coefficient	$B$	39.21	(MPa/K)	–
Reference temperature	$\theta_0$	298.15	(K)	–
Plastic parameters				
Initial yield strength	$\sigma^{lim}(\theta_0)$	150.00 $1.50 \times 10^{-6}$	(MPa) (MPa)	Solid phase Pore/Fracture phase
Constants for initial yield strength	$\omega_1$ $\omega_2$	31.00 469.82	(MPa) (K)	– –
Hardening modulus	$H(\theta_0)$	250 000.00 0.0025	(1) (1)	Solid phase Pore/Fracture phase
Constants for hardening modulus	$\omega_3$ $\omega_4$	51 741.00 469.55	(1) (K)	– –
Reference temperature	$\theta_0$	298.15	(K)	–
Thermal related properties				
Thermal conductivity	$K$	418.00 $4.18 \times 10^{-6}$	(mW/(mm × K)) (mW/(mm × K))	Solid phase Pore/Fracture phase
Specific heat capacity	$c$	$1.7 \times 10^8$ 1.70	(mJ/(T × K)) (mJ/(T × K))	Solid phase Pore/Fracture phase
Mass density	$\rho$	$1.04 \times 10^{-8}$ $1.04 \times 10^{-16}$	(T/mm <sup>3</sup> ) (T/mm <sup>3</sup> )	Solid phase Pore/Fracture phase
Initial temperature	$\theta_a$	293.15	(K)	–
Coefficient of temperature expansion	$\alpha_\theta$	$1.89 \times 10^{-5}$	(/K)	–
Phase-field parameters				
Fracture surface energy	$G_c$	0.0024	(MPa × mm)	–
Fracture length scale	$l_c$	0.0004	(mm)	–

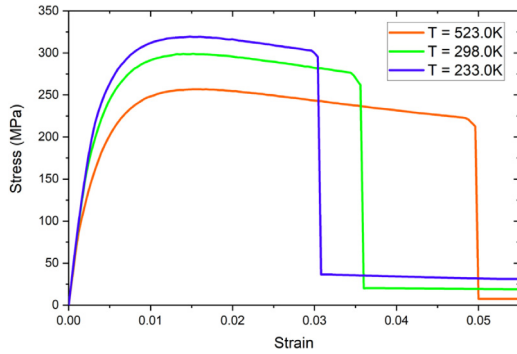


**Fig. 11.** Uniaxial tensile test results of one element under different temperature.

## 5.2. Random porous microstructures: mechanical behaviours and fracture evolutions

Aiming at the random porous microstructures, three cases are conducted to investigate the mechanical behaviours and fracture evolutions of nano-silver bulks in this subsection:

- Random porous microstructures generation and simulation. The method is thoroughly implemented and validated based on the observed micro-porous structures. Microstructure-based random porous structures can be generated and modelled to simulate the mechanical behaviours and fracture evolutions.
- Mechanical behaviours and fracture evolutions with different porosities. The effect of nano-silver sintering porosity on the mechanical behaviours and fracture evolutions is investigated. The elastic modulus, UTS and strain to failure with statistical ranges are computed by the proposed approach. Compared with the experimental results, the numerical results show good consistencies.

From these two cases, the relationships between mechanical behaviours and porosities of nano-silver bulk are studied, and the fracture topology in the random porous microstructures are predicted. Further, the numerical and experimental results are compared and discussed.

### 5.2.1. Numerical generation of random porous microstructures and simulation

As the original data of generated morphologies, a 2D microstructure image with the size of  $0.01 \times 0.01$  mm is captured from the observed nano-silver porous morphology in Fig. 1. The original image A1 is processed and transformed from the grey-scale image to the binary image. In this study, the mesh size of the phase field model is  $0.0002 \times 0.0002$  mm, which means the observed image should be compressed into  $50 \times 50$  pixels. The microstructural image is processed by python, shown in Fig. 12(a). The compressed image shows that the porosity is 0.2036 and the average length of pore size is 0.0016 mm. To describe the spatial relations of the pore phase in the compressed image, the two-point probability function of the morphology A1 is shown in Fig. 13.

Based on the processed image, the one-cut gaussian random field models are utilized to generate the synthetic random porous morphologies. The sample size of the new images is set as  $50 \times 50$  pixels. The correlation length is calculated as 8.0 pixels, which is equal to 0.0016 mm. A given amount of the random samples can therefore be obtained by gaussian random field method. Referring to the observed porosity, the one-cut levels for the different random samples are determined separately. Then, the newly-created images of S1 to S4 are obtained, shown in Fig. 12(b). Further, the two-point probability functions of the created morphologies are plotted in Fig. 13, which show a number of significant similarities with the two-point probability function of the original morphology A1. Firstly, the start points of each curve have the same value 0.2036. In addition, the two-point probability functions have the approximately same decrease rates, which indicates the similarities in the pore-phase spatial distributions. Based on the original and newly generated images, the mechanical behaviours and fracture evolutions of the random porous microstructures can be further simulated by phase field models. The digital information of original and generated images is transformed to the solid phase sets and the pore phase sets, which can be imported to the Abaqus input files for simulation.

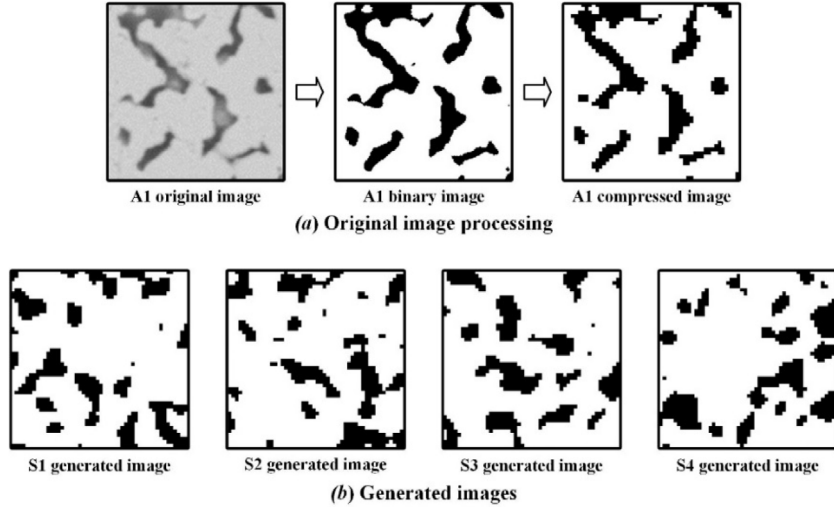


**Fig. 12.** The observed image processing and the newly generated samples S1 to S4.

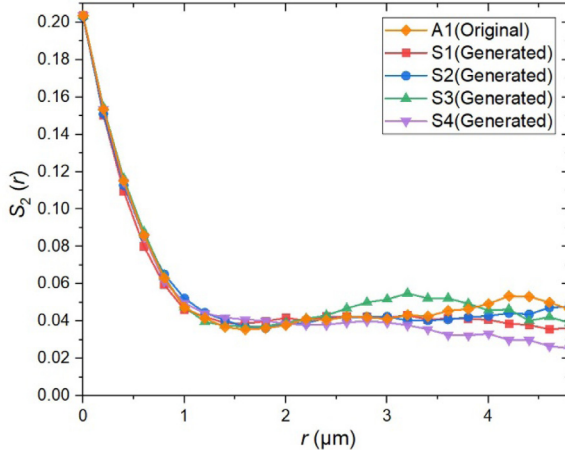


**Fig. 13.** Two-point probability functions with the original and the created morphologies.

The models of the random porous nano-silver bulks are built in Abaqus CAE. Geometry parameters and boundary conditions for tensile tests are shown in Fig. 14. The model area is  $0.01 \times 0.01$  mm, and the mesh size is 0.0002 mm. The input files without pores could be exported by Abaqus. Considering the pore phase sets and two-layer elements framework, the input files of the porous structure are reconstructed by the python codes. The new input files of the original and generated nano-silver porous bulks are imported and computed by Abaqus and its subroutines, which could analyse the mechanical behaviours and fracture evolutions of the given models.

Mechanical behaviours of the nano-silver porous bulks are simulated. From the simulation results, stress-strain curves of the real morphology A1 and the random porous morphologies S1 to S4 are obtained, shown in Fig. 15. The A1 curve is located mostly within the regional ranges among the curves of the random porous morphologies. For elastic modulus, the value range of random porous microstructures is from 25.48 GPa to 32.78 GPa, and the value of A1 is 28.06 GPa. For UTS, the value range of S1 to S4 is from 85.16 MPa to 108.30 MPa, and the value of A1 is 88.59 MPa. For strain to failure, the value range of the random micro-porous bulks is from 1.01% to 1.58%. However, the strain to failure of A1 is 0.91%, slightly lower than the given range. Due to the randomness of the synthetic micro-porous structures, the strain to failure of A1 is acceptable and reasonable for the deviation of the sampled morphologies. Hence, Fig. 15 shows the generated morphologies can be utilized to simulate the mechanical

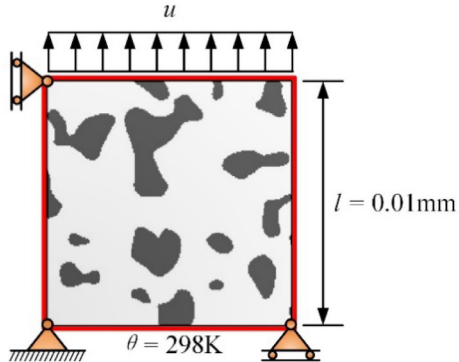


**Fig. 14.** Geometry parameters and boundary conditions for tensile tests of nano-silver porous bulks.

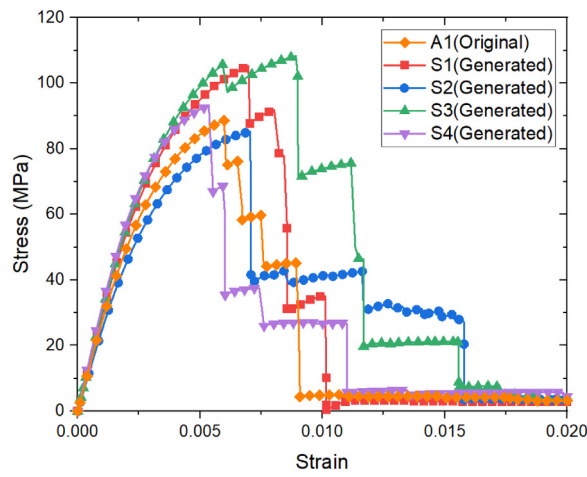


**Fig. 15.** Tensile test results of the original and generated nano-silver porous bulks.

behaviours of the real morphologies and give the reasonable value ranges of mechanical properties, including elastic modulus, UTS and strain to failure. Numerical intervals of mechanical properties could be calculated to describe the mechanical behaviours of a specific experimental micro-porous morphology.

The mechanical behaviours and fracture evolutions of A1 are calculated and obtained, as shown in Fig. 16. Six critical time points in the stress-strain curve of A1 are selected to analyse the numerical evolutions of phase field value along with the distribution evolutions of the Mises stress and maximum principal strain. There are four cracks induced in this micro-porous morphology. From Point 1 to Point 2, the first crack forms at top-right area of the morphology A1, where the local Mises stress decreases to near zero and the local maximum principal strain increases to a high level. The total stress of A1 drops sharply from 88.59 MPa to 73.96 MPa at the strain of 0.61%. The second crack generates and propagates at the top-left corner of A1 from Point 2 to Point 3. The stress region in the left of A1 almost disappears, and the high strain region at the second crack rapidly emerges. From the stress-strain curve, the strain sharply declines from 76.17 MPa to 58.35 MPa at the strain of 0.67% during the second crack forming. Then, the third crack appears at the upper right corner from Point 3 to Point 4. The stress is concentrated in the middle of A1 with these three cracks. The total stress falls 16.16 MPa suddenly at the strain of 0.76%. Finally, the micro-porous structure eventually failed due to the formation of the last crack at the upper side from Point 4 to Point 6. The strain to failure is 0.91% and the stress drops from 27.58 MPa to 4.45 MPa. From the simulation results, the Mises stress distribution of the A1 drops to zero and the maximum principal strain concentrated in the region of the cracks when the structure fails. Overall, the stress-strain curve appears discontinuous due to the relatively large ratio of the pore size to the bulk size in this small-scale model. When the cracks penetrate the pores, the micro-porous silver bulk deforms rapidly, and the curve presents multiple precipitous declines.

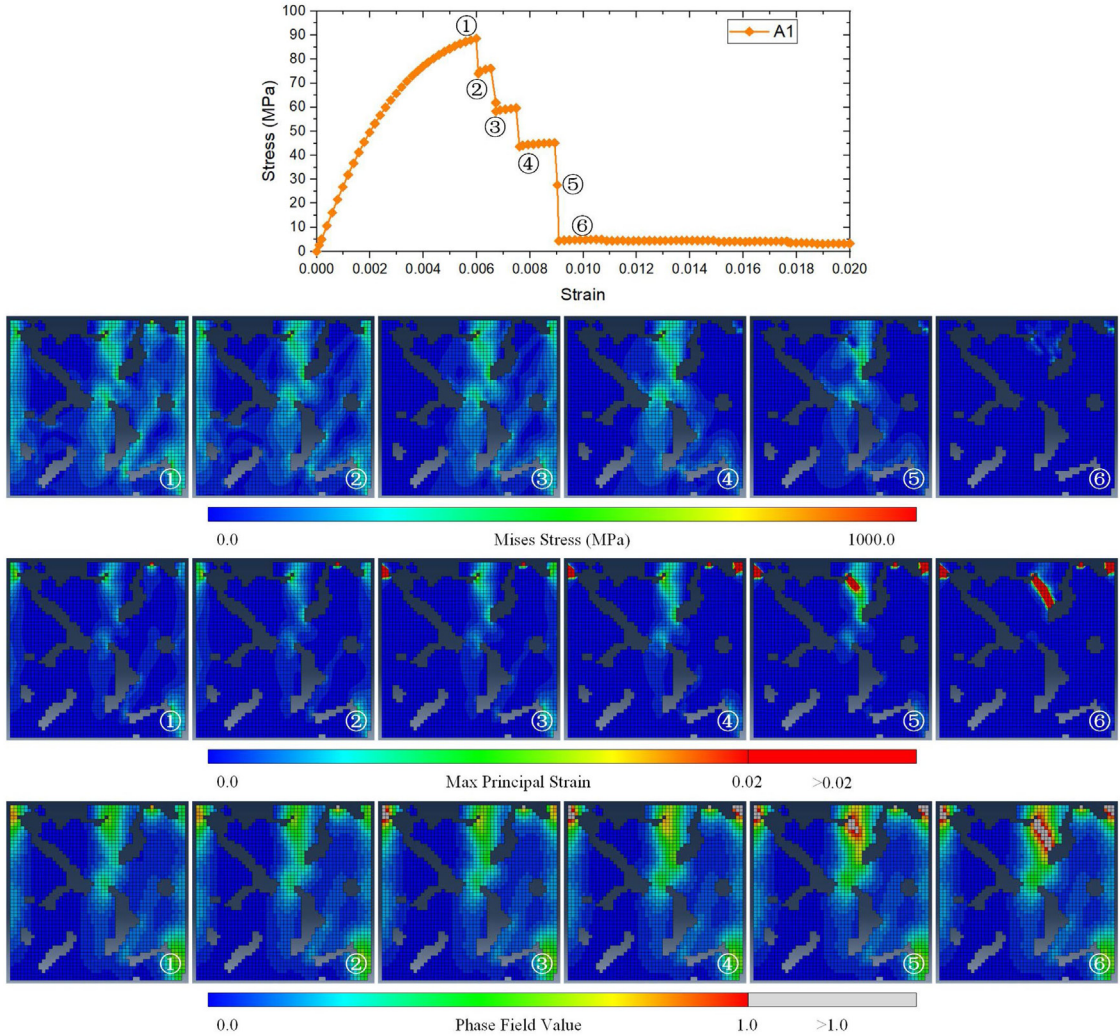


**Fig. 16.** Mechanical behaviours and fracture evolutions of A1.

Compared with the four cracks in A1, five cracks in the random morphology S3 are computed and analysed, shown in Fig. 17. Six critical time points are determined during the formation of the crack networks in S3. From Point 1 to Point 2, the first weak point breaks at the top-left corner of S3 when the strain reaches 0.61%. The Mises stress in the top-left region of S3 disappears, and the maximum principal strain at the top-left corner sharply increases. The stress decrement of the first peak in the curve is from 105.66 MPa to 97.19 MPa. Then, the second crack from Point 2 to Point 3 occurs in the right region of S3. The maximum principal strain in the crack region increases above 0.02, and the Mises stress at the right side of S3 is reduced. The total stress of S3 decreases from 108.30 MPa to 70.86 MPa at the strain of 0.90%. Next, the third crack in S3 is generated at left-top side from Point 3 to Point 4. The high strain region continues to extend along with the cracks, and the area of Mises stress is reduced further and concentrated in the middle of S3. The total stress falls from 75.65 MPa to 49.87 MPa when the total strain is 1.12%. Shortly after, the fourth crack is initiated and propagated from Point 4 to Point 5. The high strain region spreads and covers the new crack area, and the Mises stress region decreases to a small area at the right of centre. The total stress drops to 19.74 MPa at the strain of 1.17%. Eventually, the final crack in S3 emerges, forming a through crack in this micro-porous structure. From Point 5 to Point 6, the stress area is reduced to near zero, and the high strain region covers all the crack regions. At the strain to failure of 1.56%, the total stress reaches 8.89 MPa. The through cracks penetrate the pores in S3, and divide the S3 into two parts.

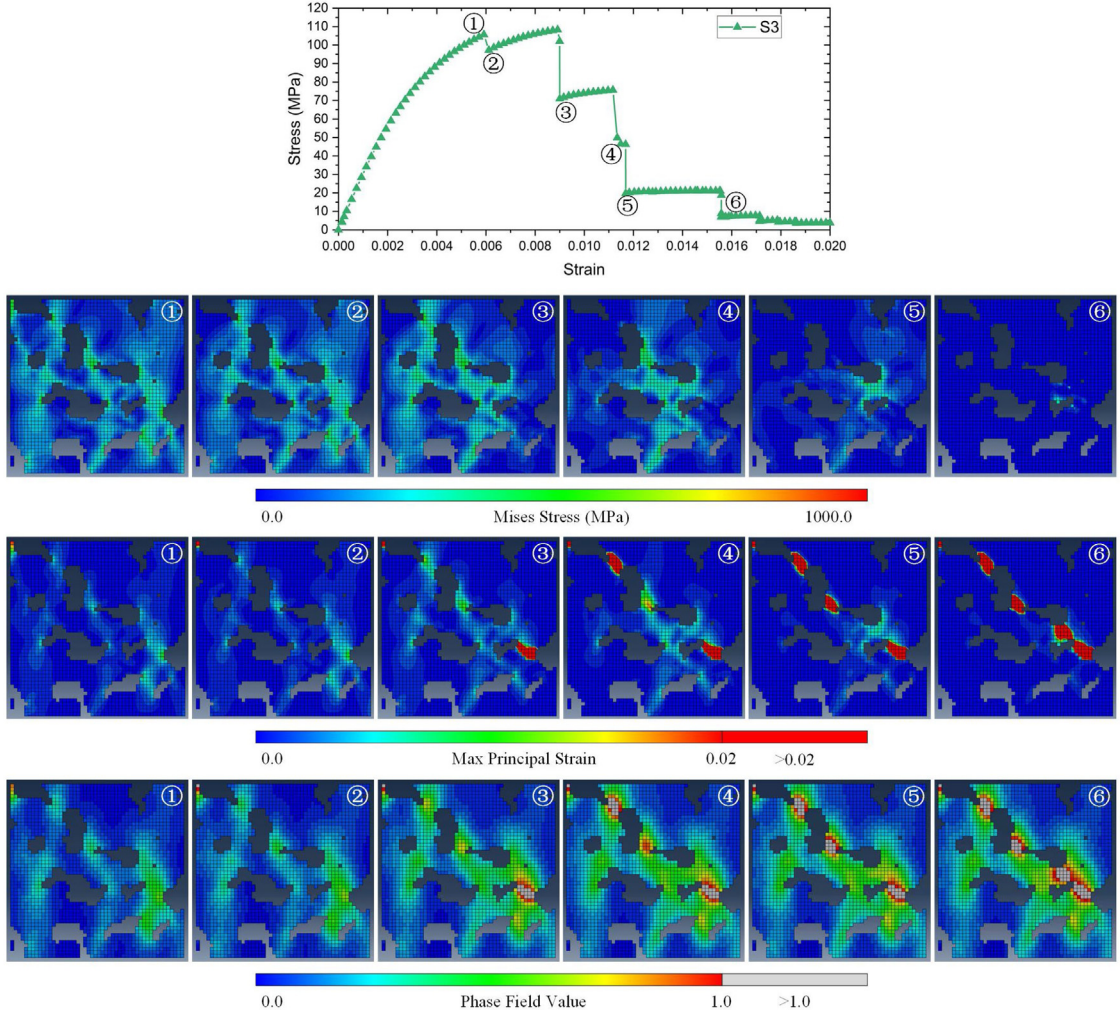


**Fig. 17.** Mechanical behaviours and fracture evolutions of S3.

Comparing the actual and created morphologies, little difference is found in the elastic moduli of these with the same porosity. However, the UTS is related to the generation of the first crack, which is also the weakest region in the morphologies. The UTS value shows a certain randomness and structural correlations of the weak region. Moreover, the strain to failure is closely related to the spatial micro-porous structure, showing strong structure-dependent and randomness during this phase field simulation. In this proposed approach, the generated micro-porous morphologies, with certain spatial characteristics and discrete randomness, can be used to simulate and predict the micro-porous materials in terms of their mechanical behaviours and random features.

#### 5.2.2. Mechanical behaviours and fracture evolutions of sintered nano-Ag with different porosities

The random micro-porous morphologies with different porosities are numerically created, simulated and discussed in this example. Five porosities of the models, including 0.10, 0.15, 0.20, 0.25, and 0.30, are selected. 25 samples with porous microstructures are randomly produced through gaussian random field, shown in Fig. 18. From these samples, the greater the porosity of the microstructure, the more complex the topographies and the larger numbers the weak regions. In particular, when the porosity of the samples is greater than 0.25, the two-dimensional morphologies are similar to complex overlapping networks. The phase field method is employed to simulate and analyse mechanical behaviours and fracture evolutions of these 25 samples. The boundary conditions are given in

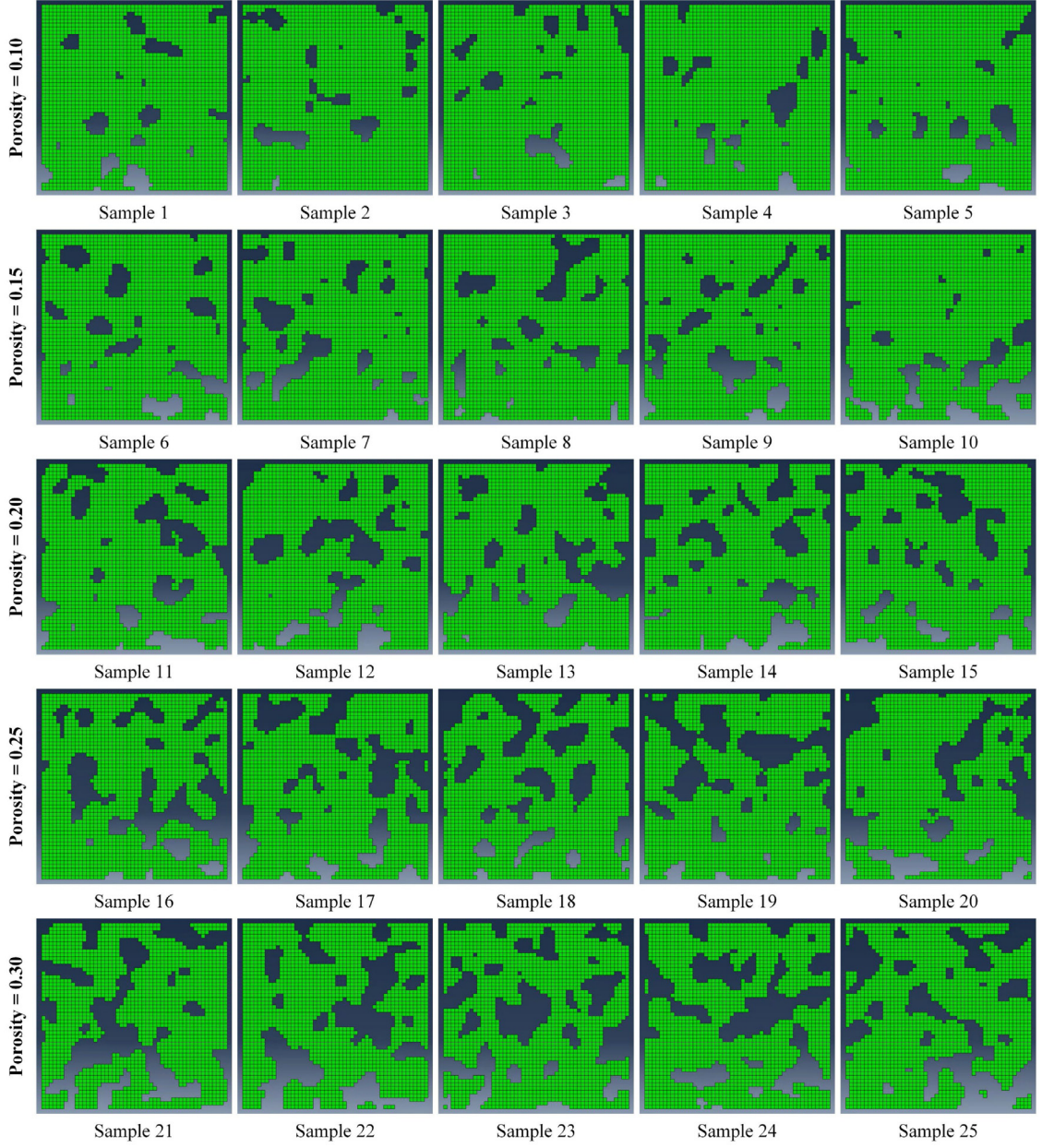


**Fig. 18.** Numerically generated random porous morphologies of sintered nano-Ag with different porosities.

**Fig. 14**, and the material parameters are listed in **Table 3**. With the results of the phase field values, the penetrating cracks from these 25 samples were obtained, as shown in **Fig. 19**. The cracks in the morphologies are formed in the weak regions, connect several adjacent pores, and divide the material bulk into two or more parts, ultimately causing the structure failure.

With the increase of the porosity, the crack number in the fracture topologies decreases, and the crack number is counted, shown in **Fig. 20(a)**. The average number of cracks in the samples is 6.4 at a porosity of 0.10, and 2.4 at a porosity of 0.30. As the porosity increases, the average number of cracks reduces progressively. The fracture topologies show that the cracks are mainly the longer ones at the smaller porosity, and the short-crack fractures occur at the necking joints between two adjacent pores when the porosity is larger. Meanwhile, as the porosity increases,

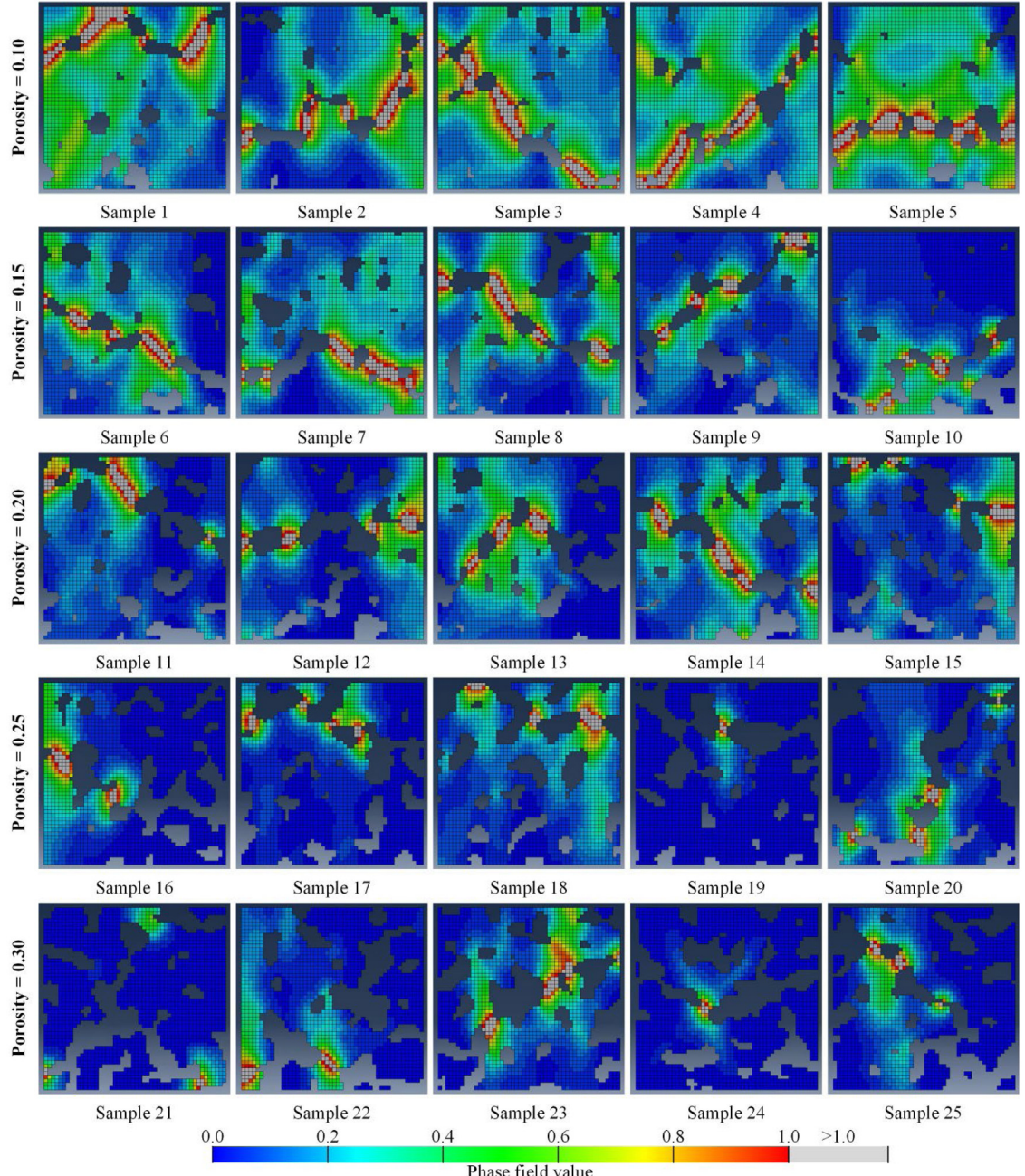


**Fig. 19.** Fracture topologies of random porous morphologies of sintered nano-Ag with different porosities.

the average length of the penetrating cracks is gradually reduced as shown in Fig. 20(b). The crack formation is related to the external energy, which is required more for the larger crack length. In other words, with the increase of the porosity, the required external energy decreases and the ductility of the porous material is reduced. Hence, the appearance features of the fracture topologies, including the crack number and length, could partly reflect the mechanical behaviour of the porous material.

The stress-strain responses of these 25 samples with different porosities are computed, shown in Fig. 21. With the increase of the porosity, the elastic modulus, UTS and strain to failure of the samples are gradually decreasing.

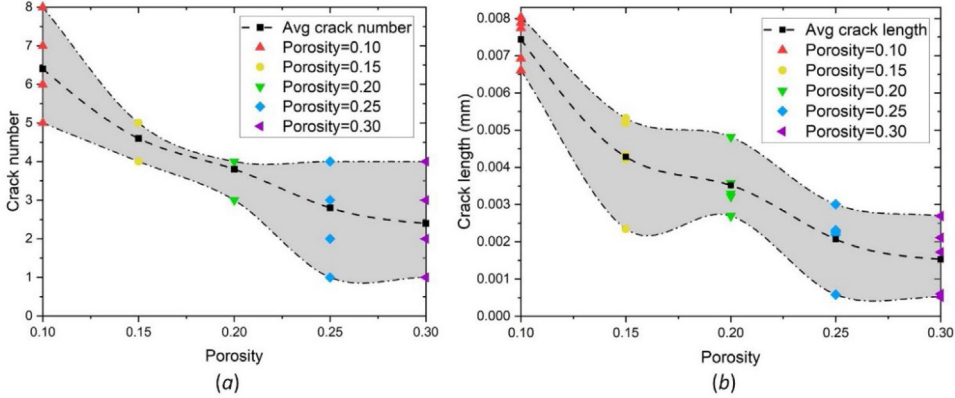


**Fig. 20.** Crack number and length for samples with different porosities.

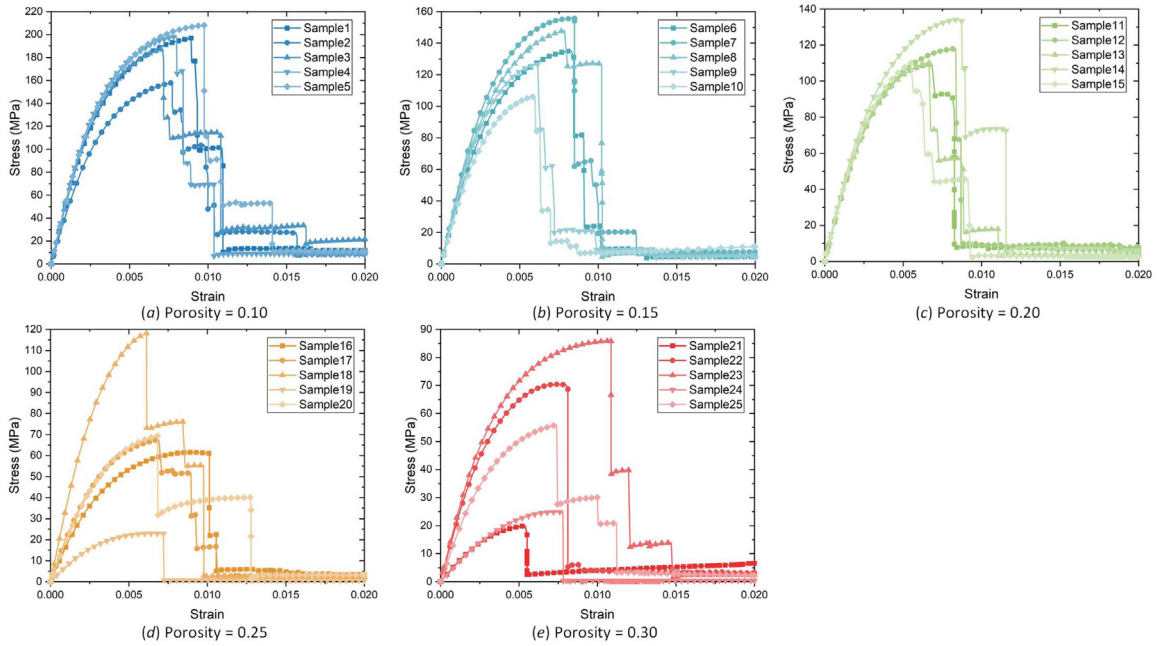


**Fig. 21.** The stress–strain responses of the generated samples with different porosities.

Meanwhile, the variances of these mechanical properties become larger. The elastic modulus is indicated at the beginning of the stress–strain curves before plastic deformation occurs. The porosity of the microstructure directly affects the initial proportion of the solid-phase and pore-phase elements, which has prominent influence on the elastic modulus. However, random spatial structure distribution has a relatively little influence on the elastic modulus. For this reason, the elastic modulus of the porous microstructure shows a steady decline with a small fluctuation as the porosity rises. With regard to the UTS, the stress strength at the first crack fracture needs to be considered. It could be obviously influenced by the random porous structure, especially the weakest point in the random structure. Overall, the strain at the first crack fracture is approximately in a certain range, the deviation of which becomes larger with the porosity rising. Before reaching the strain at the first crack fracture, the elastic and plastic moduli drop distinctly with the increase of the porosity. Therefore, the descend trend and deviations of the UTS are evidently related to the porosity and random spatial distribution. The failure point in the curves is located at the complete fracture, where the penetrating crack forms and splits the porous bulk into some fragments. The strain to failure is strongly related to the fracture topologies of the random porous structure. Less fracture energy, containing elastic

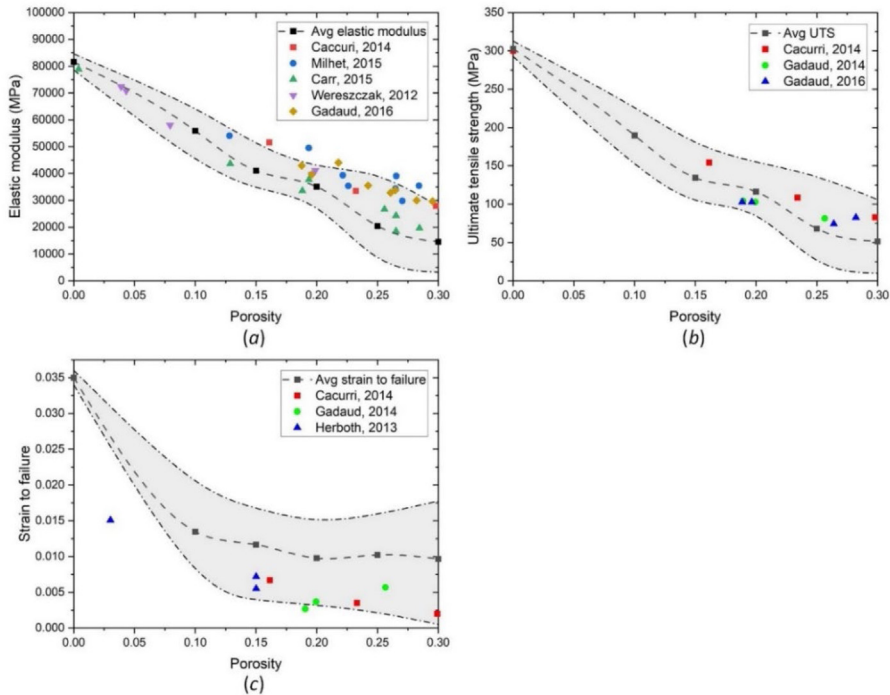


**Fig. 22.** Experimental and simulated mechanical properties of nano-silver porous bulks with different porosities [15,16,52–55].

energy, plastic energy, and temperature contribution, is required for the less cracks with smaller length and larger randomness. As the external energy is mainly provided by the upward tractions at the constant temperature, the displacement at failure, directly proportional to the strain to failure, has to be smaller to meet the lower energy requirement. Consequently, the strain to failure declines with an increasing randomness as the porosity increases.

Utilizing this phase field approach, more random samples could be simulated. As statistical results, the average values and the random fluctuation ranges of the mechanical properties, including elastic modulus, UTS and strain to failure, are obtained with the increasing porosities, shown in Fig. 22. Additionally, previous experimental results of mechanical properties for the nano-silver bulks with different porosities are also added in Fig. 22. Comparing the experimental and numerical results, the average values of the mechanical properties show the same changing tendency as the porosity rises, and the random fluctuation ranges could cover most of mechanical test results. The numerical results of elastic modulus are slightly lower than some experimental results, which can be attributed to a downward bias of the benchmark value. In terms of the UTS, the simulation results are in accordance with the experimental results, where the range of UTS by simulations could cover the UTSs of the real tensile tests. As for strain to failure, while the experimental results are within the fluctuation ranges of the numerical results, the experimental values are lower than the average values of the numerical results. There are several possible explanations for this result: (1) the different sizes of the experimental and numerical samples, (2) the different criteria for the structural failure in experiments and simulations, and (3) some spatial random factors in the simulations. More details could be explained as follows.

According to Ref. [52], the stress-strain curves under two different porosities, 0.1538 and 0.2269 respectively, are selected for further analysis. For these two porosities, more random porous microstructures are generated and simulated. Comparing with the experimental results, the simulated curves and the simulation ranges among these curves are shown in Fig. 23. It shows that the regions of simulation results could cover the experimental stress-strain curves, which located in the middle of the simulation ranges. Thus, the value ranges of the elastic modulus and UTS show good agreements with the experimental. However, the strain to failure in experiments is lower than the simulation results. There are three likely causes for the difference in the strain to failure. Firstly, the size differences between experiments and simulations may have influence on the strain to failure. Due to the different length scale, the experimental samples in the macro scale show a rapid ultimate fracture shortly before reaching the UTS, without

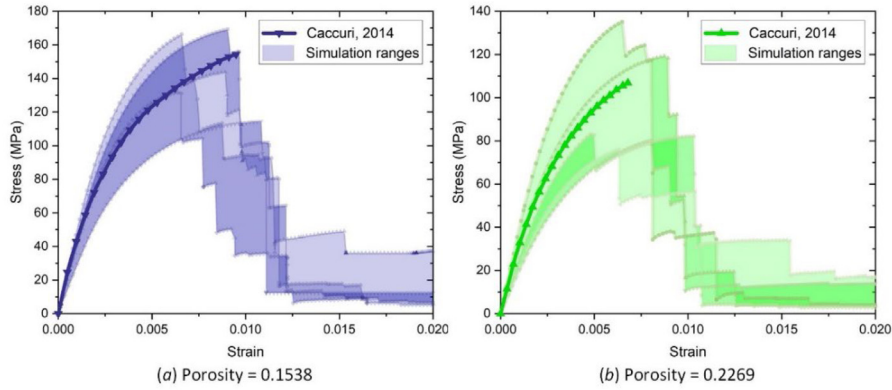


**Fig. 23.** The stress–strain curves of experiments and simulations under two different porosities.

any staged precipitous drops. The staged drops in the simulation results could extend the strain at complete fracture. Secondly, the structural failure criteria of the experiments may be different from that of the simulations. In the simulations, the penetrating cracks, connecting the pores and dividing the bulks into two or more fragments, are deemed as the failure criteria, similar to those shown in Fig. 19. However, the phenomenological failure criteria, which assumes a material fails when the maximum principal stress exceeds the ultimate tensile strength, is adopted in the uniaxial tensile tests. Because of this, the strain to failure in the experiments is smaller than that in the simulations. Thirdly, some spatial randomness of the microstructures should be considered. Due to the randomly generated micro-porous structures, the strain to failure is easily affected by the randomness, resulting in a certain bias in the simulation results. In summary, the simulation results focus on the micro-scale porous morphologies, instead of the macro-scale ones. And more detailed ductility in the micro-scale could be modelled and obtained in the simulations.

### 5.3. Nano-silver sintering structure: thermal cyclic test and crack networks analysis

The main aim of this numerical example is to verify the thermo-elasto-plastic phase field method in order to solve the coupled thermomechanical problems with complex crack networks in random porous nano-silver structures. The typical sintered nano-silver structure is obtained from the die-attach in assembled power modules. Referring to [56], the two-dimensional sintered nano-silver structure under a single heat point is used.

The geometry parameters and boundary conditions of this structure are shown in Fig. 24. Assuming the single heat point in the model is located in the middle with the heat power equivalent to the multiple heating across the entire chip, the structure under this heat point had approximate symmetries on both left side and right side, where the horizontal degrees of freedom of the left-side and right-side boundaries are restricted to zero. The bottom of the structure is fixed at the initial position. The three heat boundary conditions are considered in this model, containing thermal insulations on the top, left-side and right-side of the structure, a heat point at the top centre, and a surface-based film mimicking the heat sink condition at the bottom. The film temperature value is set 293.15 K, and the film coefficient is an adjustable parameter to tighten or ease the thermal conditions, given a value of 1.5 J/(s K mm<sup>2</sup>).

This stacked structure from top to bottom contains silicon chip, sintered nano-silver layer, the first copper, AlN ceramic, and the second copper layer. The material properties of the chip, copper, and ceramic in this model are given in Table 4, and the material setting of sintered nano-silver is shown in Table 3. As seen in Fig. 24, the sintered nano-silver porous microstructure with a porosity of 18% is obtained based on the random gaussian field methods. And the elements in the solid sintered silver layer are set as phase field elements, which is utilized to analyse the complex fracture evolutions in this porous microstructure.

For the phase field elements, two layers of the sintered nano-silver porous elements are determined, containing 100×1000 coupled temperature–displacement quadrilateral elements and 100 × 1000 UEL quadrilateral elements. The other material structures are only the coupled temperature–displacement elements, including 20,180 quadrilateral and 64,300 triangular ones.

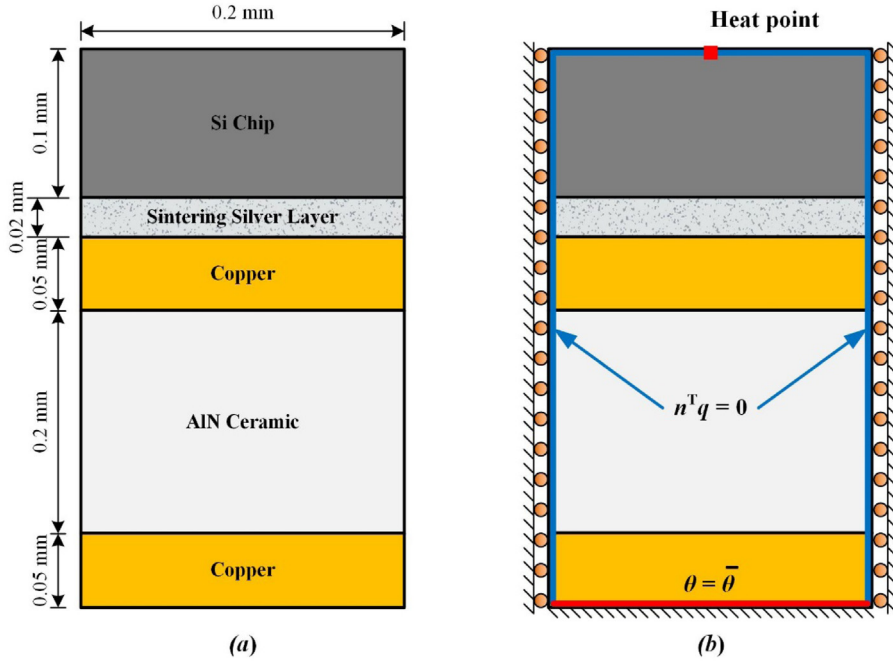


**Fig. 24.** Geometry parameters and boundary conditions for die-attach in power modules under a single heat point.

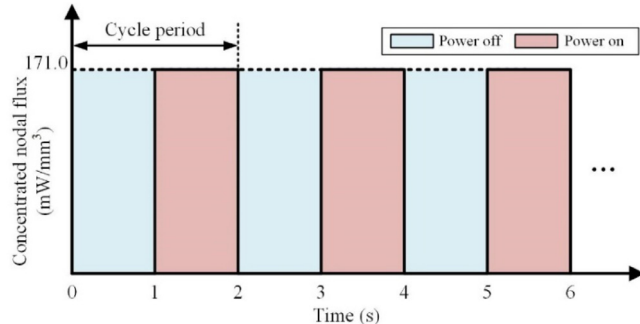


**Fig. 25.** Thermal cyclic profile of the heat point at the top of the model.

**Table 4**

Material properties of silicon chip, copper, and AlN ceramic in the model (Ref. [57]).

Parameter	Silicon chip	Copper	AlN ceramic
Young's modulus (MPa)	162 000.00	110 000.00	348 000.00
Poisson's ratio	0.28	0.35	0.27
Thermal conductivity (mW/(mm × K))	130.00	400.00	177.00
Specific heat capacity (mJ/(T × K))	$7.00 \times 10^8$	$3.85 \times 10^8$	$8.20 \times 10^8$
Mass density (T/mm <sup>3</sup> )	$2.33 \times 10^{-9}$	$8.96 \times 10^{-9}$	$3.34 \times 10^{-9}$
Coefficient of temperature expansion (/K)	$3.00 \times 10^{-6}$	$1.70 \times 10^{-5}$	$5.60 \times 10^{-6}$

The heat point at the top of this model is set as a concentrated nodal flux, the thermal cyclic profile of which is shown in Fig. 25. The concentrated nodal flux of the power module is assumed as a square wave function where the maximum, minimum and frequency values are 171.0 mW/mm<sup>3</sup>, 0.0 mW/mm<sup>3</sup> and 0.5 Hz, respectively. 50 cycles of the thermal cyclic conditions are totally applied to this heat point to investigate the fracture evolutions

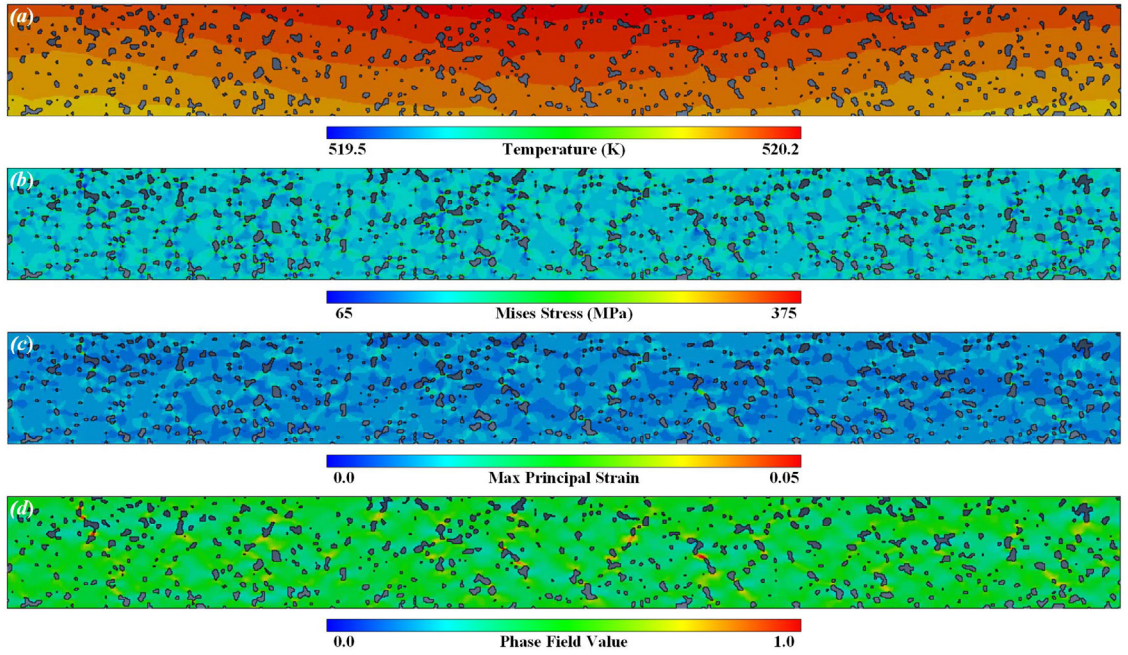


**Fig. 26.** The distributions of temperature, Mises stress, maximum principal strain and phase field value before fracture initiation.

and crack networks in the sintered nano-silver micro-porous structures. Through Abaqus and its subroutines, the phase field calculations demand 4550 times of increments in total.

Before the first failed element appears at the 50th increment, the distributions of temperature, Mises stress, maximum principal strain and phase field value are obtained as shown in Fig. 26. The temperature distribution ranging from 519.5 K to 520.2 K shows that the temperature gradually decreases from the highest at the heat point downwards in Fig. 26(a). The pore phase in the model can influence the thermal behaviour due to the poor thermal conductivity. For Mises stress distribution, the stresses between the pores are interconnected to form a distributed stress network, shown in Fig. 26(b). The stresses are prone to be concentrated between the adjacent pores, where cracking is likely to initiate. Further, Fig. 26(c) shows the distribution of the maximum principal strain, and reveals the strain values at each material point. High strain values combined with high stress values in the same material points lead to high phase field values due to the energy functions. The phase field distribution presents a similar trend in the strain distribution, shown in Fig. 26(d). The subsequent simulations indicate that the fractures in the micro-porous structure initiate in the positions at high phase field values.

After 4550 time increments, there are five noticeable longitudinal cracks forming in the sintered silver layer based on the phase field value, shown in Fig. 27. The formation of the cracks in the micro-porous structure under thermal cyclic conditions can be divided into three stages. Firstly, the neighbouring pores in the centre area are vertically connected each other through the micro-cracks, forming the initial cracks. Then, the initial cracks propagate longitudinally towards the top and bottom through connecting the pores, and penetrate the porous structure from the chip-side at the top downwards. The cracks evolve in the second stage into longitudinal through-cracking. Once longitudinal penetration cracks occur, the cracks begin to extend alongside the top or bottom interface horizontally. Finally, the complex crack networks are formed, bridging the pores along the vertical and horizontal directions in the sintered nano-silver layer. The formation process of the five visible cracks in the crack networks are shown in Fig. 27. The staged time points of the five cracks are located in the total time increments of this simulation. The crack 4, located on the slightly right side of the centre of the sintered nano-Ag, has the shortest time to penetrate through the nano-Ag layer from increment 51 to 167, and the crack 1, located on the left side, has the longest time to penetrate from increment 51 to 298. Even though, the results of this phase field model for random porous nano-silver structure show no significant relationship between cracking time and location.

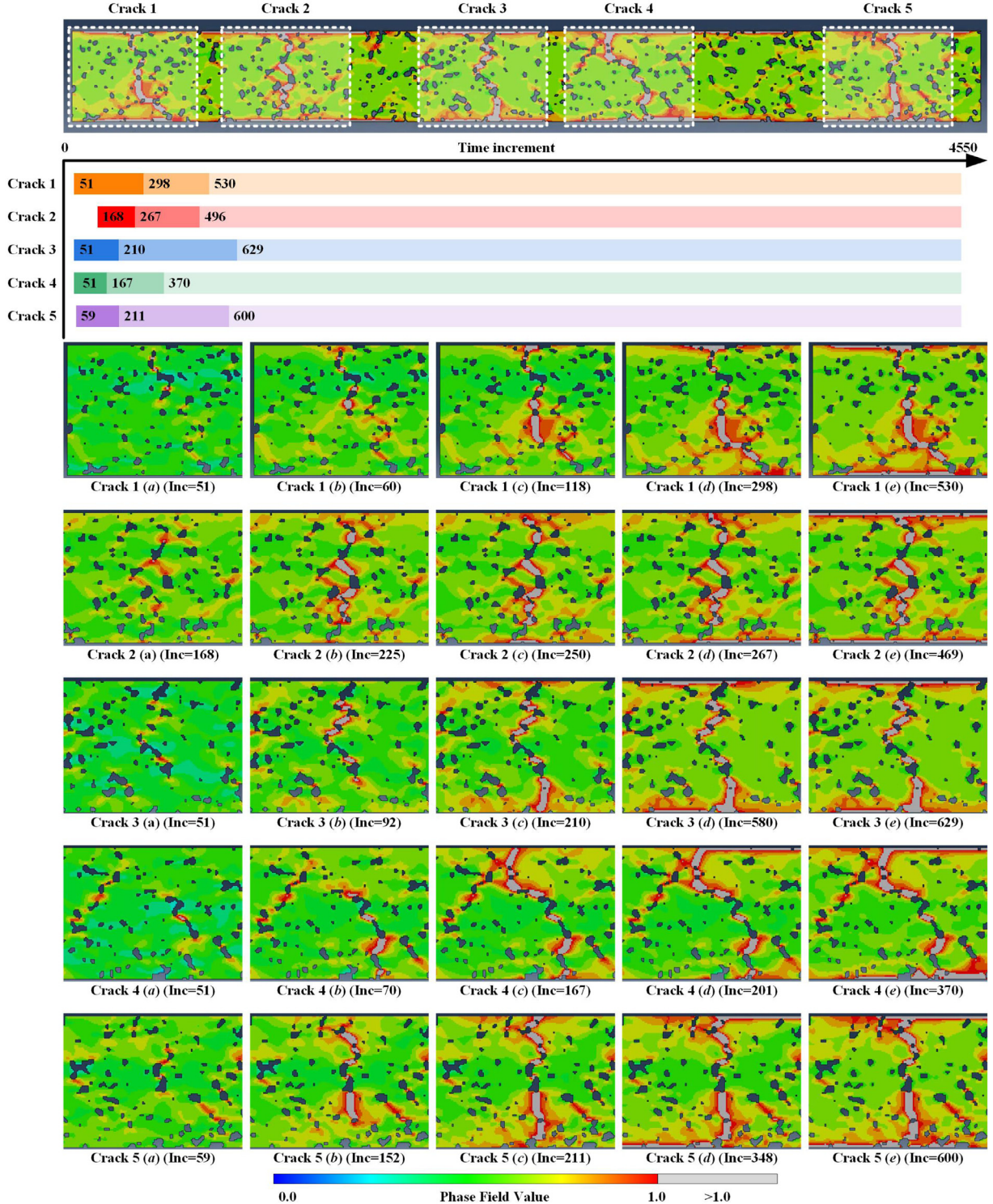


**Fig. 27.** The formation of the crack networks consisting of five noticeable cracks in the sintered nano-silver micro-porous structure.

Moreover, the numerical results of the crack patterns and networks agree with the findings of other experimental studies [56,58], shown in Fig. 28. Fig. 28(a) shows there are four types of crack topologies, including T-shaped

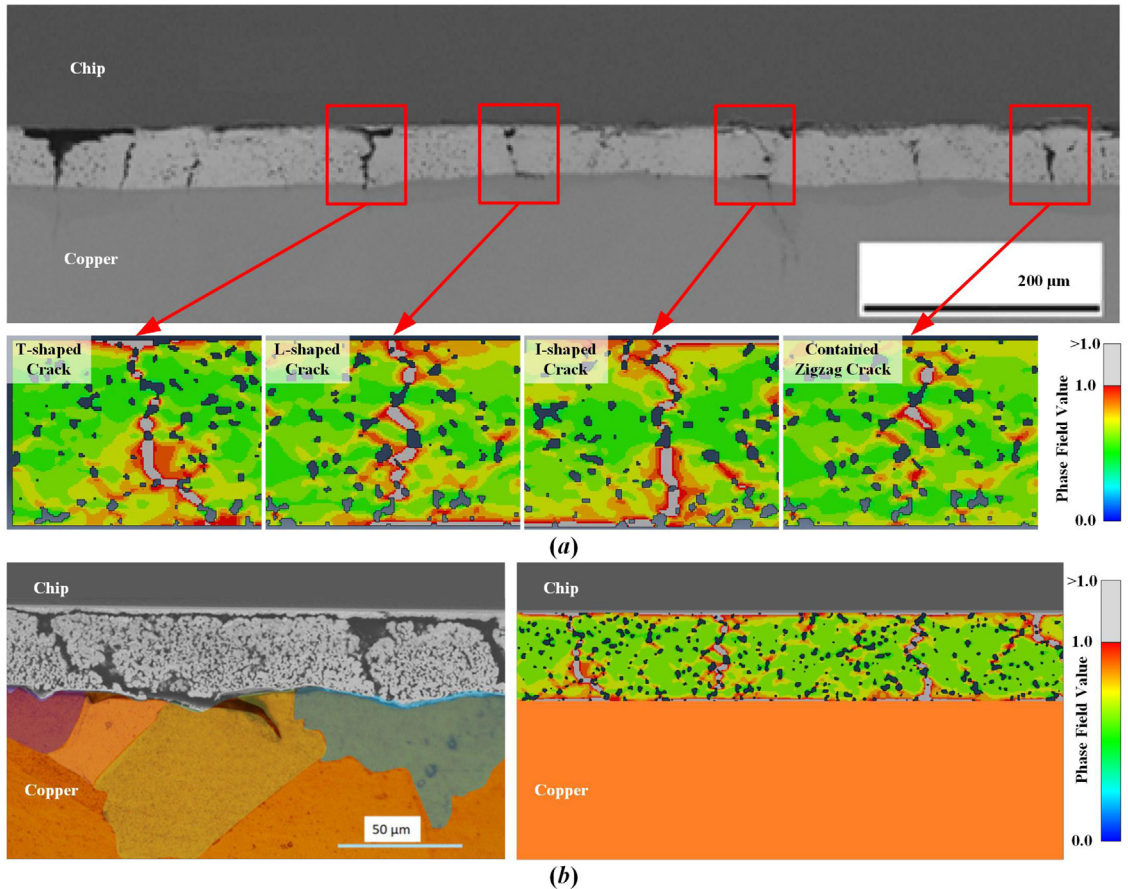


**Fig. 28.** The comparison between the numerical and experimental results of the crack patterns and networks [56,58].

crack, L-shaped crack, I-shaped crack and contained zigzag crack, in both experiments and phase field simulations. The contained zigzag cracks are commonly found in the initial stage of cracking by connecting limited number of near-by pores. The T-shaped or L-shaped cracks occur after the formation of the penetration cracks, extending along either of the top or bottom interfaces in the porous structures. When the penetration cracks propagate on both bottom and top side, or the T-shaped or L-shaped cracks develop along the other non-cracked interface, I-shaped crack could be formed across the sintered layer longitudinally. Further, Fig. 28(b) presents the intersections of multiple I-shaped cracks in both experiments and simulations, forming the complex crack networks in the sintered layer. Multiple vertical penetrating cracks connecting the two horizontal cracks at the top and bottom interfaces comprise the ladder-shaped crack networks, resulting in reduced structural strength, increased thermal resistance or even open circuit.

## 6. Conclusions

In this paper, we proposed a computational framework combining the random gaussian field method with thermo-elasto-plastic phase field model to simulate the mechanical behaviours and fracture evolutions of sintered nano-silver structures with randomly distributed micro-pores. The contribution of this study has been to provide a novel approach to statistical analysis of the mechanical responses of the micro-porous sintered nano-Ag structures to the thermo-elasto-plastic conditions, hence, simulate the fracture evolutions due to the formations of crack networks in the micro-porous systems under thermal cyclic conditions. One of the significant findings emerging from this study is that the developed phase field model for the random porous materials is able to evaluate the mechanical behaviours with fluctuation regions, thus establish a statistical relationship between the porosity and the mechanical properties,

including elastic modulus, UTS and strain to failure. Another interesting finding in this study is that fracture evolutions in the sintered nano-silver micro-porous structures under thermal cyclic conditions can be visualized in detail using the combined phase field method established. Diverse patterns of initiated cracks are also derived with the four types of crack formation identified at the different regions in the sintered nano-Ag structures, i.e. T-shaped, L-shaped, I-shaped and contained zigzag crack. Further, the phase field simulations have yielded the complex crack networks in the form of ladder-shaped cracking path through the sintered nano-Ag layer, which shows the excellent consistencies with the experimental observation from the similar systems. Two-dimensional phase field simulations for this random porous material were implemented to reduce the amount of meshes and improve the computing efficiency. To ensure the accuracy of two-dimensional phase field model, numerical experiments for single element and random porous material bulks were conducted, which shows a good agreement with the experimental results. Overall, this newly established numerical simulation platform is capable of encompassing wide range variables involved in the real-life loading conditions to elaborate the mechanical properties of the randomly porous materials, and to improve the understandings of the fracture evolutions due to the initiation and propagation of cracks to form the networks in the sintered nano-silver.

In this study, we focus more on the micro-scale modelling for the nano-silver micro-porous structures. Further research can be carried out to establish a multi-scale computational model which may consider the statistical properties of the mechanical behaviours based on the random heterogeneous methods. And other degradation mechanisms, such as grain coarsening and migration, could also be considered to establish a multi-phase field method. Moreover, the current approach can be developed to solve the three-dimensional problems of the mechanical behaviours and fracture evolutions of the randomly distributed micro-porous structures, which will demand a significant computational power to complete the tasks.

### Declaration of competing interest

The authors declare that they have no known competing financial interests or personal relationships that could have appeared to influence the work reported in this paper.

### Acknowledgements

The authors acknowledge the funding supports provided by the China Scholarship Council (CSC) (Reference No. 201906020125), and the EPSRC research grants (UK): (i) Underpinning Power Electronics 2017 - Heterogeneous Integration (HI) project (Grant No. EP/R004501/1), and (ii) Quasi-ambient bonding to enable cost-effective high temperature Pb-free solder interconnects (QAB) project (Grant No. EP/R032203/1). The authors thank Dr Stuart Robertson and Dr Zhaoxia Zhou of Loughborough University for their thoughtful discussions and suggestions in this study.

### References

- [1] V.R. Manikam, K.Y. Cheong, Die attach materials for high temperature applications: A review, *IEEE Trans. Compon. Packag. Manuf. Technol.* 1 (2011) 457–478.
- [2] C.T. Chen, C.Y. Choe, Z. Zhang, D.J. Kim, K. Suganuma, Low-stress design of bonding structure and its thermal shock performance (-50 to 250 °C) in SiC/DBC power die-attached modules, *J. Mater. Sci. Mater. Electron.* 29 (2018) 14335–14346.
- [3] H.Q. Zhang, W.G. Wang, H.L. Bai, G.S. Zou, L. Liu, P. Peng, W. Guo, Microstructural and mechanical evolution of silver sintering die attach for SiC power devices during high temperature applications, *J. Alloy. Compd.* 774 (2019) 487–494.
- [4] C. Chen, C. Choe, D. Kim, K. Suganuma, Lifetime prediction of a SiC power module by Micron/Submicron Ag sinter joining based on fatigue, creep and thermal properties from room temperature to high temperature, *J. Electron. Mater.* (2020).
- [5] S.A. Paknejad, S.H. Mannan, Review of silver nanoparticle based die attach materials for high power/temperature applications, *Microelectron. Reliab.* 70 (2017) 1–11.
- [6] S. Soichi, K. Suganuma, Low-temperature and low-pressure die bonding using thin ag-flake and ag-particle pastes for power devices, *IEEE Trans. Compon. Pack. Manuf. Technol.* 3 (2013) 923–929.
- [7] H. Alarifi, A. Hu, M. Yavuz, Y.N. Zhou, Silver nanoparticle paste for low-temperature bonding of copper, *J. Electron. Mater.* 40 (2011) 1394–1402.
- [8] K.S. Siow, *Die-Attach Materials for High Temperature Applications in Microelectronics Packaging*, Springer, 2019.
- [9] F. Yang, W. Zhu, W. Wu, H. Ji, C. Hang, M. Li, Microstructural evolution and degradation mechanism of SiC-Cu chip attachment using sintered nano-Ag paste during high-temperature ageing, *J. Alloy. Compd.* 846 (2020) 156442.
- [10] Y. Liu, H. Zhang, L. Wang, X. Fan, G. Zhang, F. Sun, Effect of sintering pressure on the porosity and the shear strength of the pressure-assisted silver sintering bonding, *IEEE Trans. Device Mater. Reliab.* (2018) 1.

- [11] F. Qin, Y. Hu, Y. Dai, T. An, P. Chen, Y. Gong, H. Yu, Crack effect on the equivalent thermal conductivity of porously sintered silver, *J. Electron. Mater.* 49 (2020) 5994–6008.
- [12] C. Weber, M. Hutter, S. Schmitz, K. Lang, Dependency of the porosity and the layer thickness on the reliability of Ag sintered joints during active power cycling, in: 2015 IEEE 65th Electronic Components and Technology Conference (ECTC), 2015, pp. 1866–1873.
- [13] R. Kimura, Y. Kariya, N. Mizumura, K. Sasaki, Effect of sintering temperature on fatigue crack propagation rate of sintered Ag nanoparticles, *Mater. Trans.* 59 (2018) 612–619.
- [14] K. Wakamoto, Y. Mochizuki, T. Otsuka, K. Nakahara, T. Namazu, Tensile mechanical properties of sintered porous silver films and their dependence on porosity, *Japan. J. Appl. Phys.* 58 (2019) SDDL08.
- [15] A.A. Wereszczak, D.J. Vuono, H. Wang, M.K. Ferber, Z. Liang, Properties of Bulk Sintered Silver As a Function of Porosity, in, Oak Ridge National Lab.(ORNL), Oak Ridge, TN (United States, 2012).
- [16] J. Carr, X. Milhet, P. Gadaud, S.A.E. Boyer, G.E. Thompson, P. Lee, Quantitative characterization of porosity and determination of elastic modulus for sintered micro-silver joints, *J. Mater Process. Technol.* 225 (2015) 19–23.
- [17] Y. Yao, Q. Huang, S. Wang, Effects of porosity and pore microstructure on the mechanical behavior of nanoporous silver, *Mater. Today Commun.* (2020) 101236.
- [18] Z. Chen, X. Wang, F. Giuliani, A. Atkinson, Microstructural characteristics and elastic modulus of porous solids, *Acta Mater.* 89 (2015) 268–277.
- [19] C. Soyarslan, M. Pradas, S. Bargmann, Effective elastic properties of 3D stochastic bicontinuous composites, *Mech. Mater.* 137 (2019) 103098.
- [20] S.S. Vel, A.J. Goupee, Multiscale thermoelastic analysis of random heterogeneous materials: Part I: Microstructure characterization and homogenization of material properties, *Comput. Mater. Sci.* 48 (2010) 22–38.
- [21] A. Gillman, M. Roelofs, K. Matouš, V. Kouznetsova, O. van der Sluis, M. van Maris, Microstructure statistics–property relations of silver particle-based interconnects, *Mater. Des.* 118 (2017) 304–313.
- [22] J. Fang, C. Wu, T. Rabczuk, C. Wu, C. Ma, G. Sun, Q. Li, Phase field fracture in elasto-plastic solids: Abaqus implementation and case studies, *Theor. Appl. Fract. Mech.* 103 (2019) 102252.
- [23] T. Wang, X. Ye, Z. Liu, X. Liu, D. Chu, Z. Zhuang, A phase-field model of thermo-elastic coupled brittle fracture with explicit time integration, *Comput. Mech.* 65 (2020) 1305–1321.
- [24] C. Miehe, L.M. Schanzel, H. Ulmer, Phase field modeling of fracture in multi-physics problems. Part I. Balance of crack surface and failure criteria for brittle crack propagation in thermo-elastic solids, *Comput. Methods Appl. Mech. Engrg.* 294 (2015) 449–485.
- [25] M. Dittmann, F. Aldakheel, J. Schulte, F. Schmidt, M. Krüger, P. Wriggers, C. Hesch, Phase-field modeling of porous-ductile fracture in non-linear thermo-elasto-plastic solids, *Comput. Methods Appl. Mech. Engrg.* 361 (2020) 112730.
- [26] M. Krüger, M. Dittmann, F. Aldakheel, A. Härtel, P. Wriggers, C. Hesch, Porous-ductile fracture in thermo-elasto-plastic solids with contact applications, *Comput. Mech.* 65 (2020) 941–966.
- [27] C. Miehe, M. Hofacker, L.M. Schanzel, F. Aldakheel, Phase field modeling of fracture in multi-physics problems. Part II. Coupled brittle-to-ductile failure criteria and crack propagation in thermo-elastic–plastic solids, *Comput. Methods Appl. Mech. Engrg.* 294 (2015) 486–522.
- [28] C. Miehe, H. Dal, L.M. Schanzel, A. Raina, A phase-field model for chemo-mechanical induced fracture in lithium-ion battery electrode particles, *Internat. J. Numer. Methods Engrg.* 106 (2016) 683–711.
- [29] T.T. Nguyen, D. Waldmann, T.Q. Bui, Computational chemo-thermo-mechanical coupling phase-field model for complex fracture induced by early-age shrinkage and hydration heat in cement-based materials, *Comput. Methods Appl. Mech. Engrg.* 348 (2019) 1–28.
- [30] C. Miehe, S. Mauthe, Phase field modeling of fracture in multi-physics problems. Part III. Crack driving forces in hydro-poro-elasticity and hydraulic fracturing of fluid-saturated porous media, *Comput. Methods Appl. Mech. Engrg.* 304 (2016) 619–655.
- [31] W. Ehlers, C. Luo, A phase-field approach embedded in the theory of porous media for the description of dynamic hydraulic fracturing, *Comput. Methods Appl. Mech. Engrg.* 315 (2017) 348–368.
- [32] S. Zhou, X. Zhuang, T. Rabczuk, Phase-field modeling of fluid-driven dynamic cracking in porous media, *Comput. Methods Appl. Mech. Engrg.* 350 (2019) 169–198.
- [33] J. Cho, K.-S. Lee, Finite element simulation of crack propagation based on phase field theory, *J. Mech. Sci. Technol.* 27 (2013) 3073–3085.
- [34] U. Pillai, Y. Heider, B. Markert, A diffusive dynamic brittle fracture model for heterogeneous solids and porous materials with implementation using a user-element subroutine, *Comput. Mater. Sci.* 153 (2018) 36–47.
- [35] J. Carlsson, P. Isaksson, A statistical geometry approach to length scales in phase field modelling of fracture and strength of porous microstructures, *Int. J. Solids Struct.* (2020).
- [36] M. Schaal, M. Klingler, B. Wunderle, Silver sintering in power electronics: The state of the art in material characterization and reliability testing, in: 2018 7th Electronic System-Integration Technology Conference (ESTC), 2018, pp. 1–18.
- [37] C. Liu, F. Mohn, J. Schuderer, D. Torresin, Novel large-area attachment for high-temperature power electronics module application, in: 2017 IEEE 67th Electronic Components and Technology Conference (ECTC), 2017, pp. 1547–1552.
- [38] S. Nishimoto, S.A. Moeini, T. Ohashi, Y. Nagatomo, P. McCluskey, Novel silver die-attach technology on silver pre-sintered DBA substrates for high temperature applications, *Microelectron. Reliab.* 87 (2018) 232–237.
- [39] P. Liu, G.-F. Chen, Porous Materials: Processing and Applications, Elsevier, 2014.
- [40] R. Durrett, Probability: Theory and Examples, Cambridge university press, 2019.
- [41] S. Torquato, Random Heterogeneous Materials: Microstructure and Macroscopic Properties, Springer Science & Business Media, 2013.
- [42] A.P. Roberts, M. Teubner, Transport properties of heterogeneous materials derived from Gaussian random fields: bounds and simulation, *Phys. Rev. E* 51 (1995) 4141.

- [43] C. Miehe, F. Welschinger, M. Hofacker, Thermodynamically consistent phase-field models of fracture: Variational principles and multi-field FE implementations, *Internat. J. Numer. Methods Engrg.* 83 (2010) 1273–1311.
- [44] G. Molnár, A. Gravouil, 2d and 3D abaqus implementation of a robust staggered phase-field solution for modeling brittle fracture, *Finite Elem. Anal. Des.* 130 (2017) 27–38.
- [45] O.L. Anderson, Derivation of wachtman's equation for the temperature dependence of elastic moduli of oxide compounds, *Phys. Rev.* 144 (1966) 553–557.
- [46] J.B. Wachtman, W.E. Tefft, D.G. Lam, C.S. Apstein, Exponential temperature dependence of Young's modulus for several oxides, *Phys. Rev.* 122 (1961) 1754–1759.
- [47] G. Molnar, A. Gravouil, R. Seghir, J. Rethore, An open-source abaqus implementation of the phase-field method to study the effect of plasticity on the instantaneous fracture toughness in dynamic crack propagation, *Comput. Methods Appl. Mech. Engrg.* 365 (2020) 113004.
- [48] R.V. Mises, Mechanik der festen Körper im plastisch-deformablen Zustand, *Nachrichten von der Gesellschaft der Wissenschaften zu Göttingen, Mathematisch-Physikalische Klasse* 1913 (1913) 582–592.
- [49] D.J. Bammann, Modeling temperature and strain rate dependent large deformations of metals, *Appl. Mech. Rev.* 43 (1990) S312–S319.
- [50] O.C. Zienkiewicz, R.L. Taylor, *The Finite Element Method for Solid and Structural Mechanics*, Elsevier, 2005.
- [51] K. Sugiura, T. Iwashige, K. Tsuruta, C.T. Chen, S. Nagao, T. Funaki, K. Suganuma, Reliability evaluation of SiC power module with sintered Ag die attach and stress-relaxation structure, *IEEE Trans. Compon. Pack. Manuf. Technol.* 9 (2019) 609–615.
- [52] V. Caccuri, X. Milhet, P. Gadaud, D. Bertheau, M. Gerland, Mechanical properties of sintered Ag as a new material for die bonding: influence of the density, *Journal of electronic materials* 43 (2014) 4510–4514.
- [53] P. Gadaud, V. Caccuri, D. Bertheau, J. Carr, X. Milhet, Ageing sintered silver: Relationship between tensile behavior, mechanical properties and the nanoporous structure evolution, *Mater. Sci. Eng. A* 669 (2016) 379–386.
- [54] X. Milhet, P. Gadaud, V. Caccuri, D. Bertheau, D. Mellier, M. Gerland, Influence of the porous microstructure on the elastic properties of sintered Ag paste as replacement material for die attachment, *J. Electron. Mater.* 44 (2015) 3948–3956.
- [55] T. Herboth, M. Guenther, A. Fix, J. Wilde, Failure mechanisms of sintered silver interconnections for power electronic applications, in: 2013 IEEE 63rd Electronic Components and Technology Conference, IEEE, 2013, pp. 1621–1627.
- [56] J. Dai, J. Li, P. Agyakwa, M. Corfield, C.M. Johnson, Comparative thermal and structural characterization of sintered nano-silver and high-lead solder die attachments during power cycling, *IEEE Trans. Device Mater. Reliab.* 18 (2018) 256–265.
- [57] B. Hu, J.O. Gonzalez, L. Ran, H. Ren, Z. Zeng, W. Lai, B. Gao, O. Alatise, H. Lu, C. Bailey, P. Mawby, Failure and reliability analysis of a SiC power module based on stress comparison to a si device, *IEEE Trans. Device Mater. Reliab.* 17 (2017) 727–737.
- [58] P. Agyakwa, J. Dai, J. Li, B. Mouawad, L. Yang, M. Corfield, C. Johnson, Three-dimensional damage morphologies of thermomechanically deformed sintered nanosilver die attachments for power electronics modules, *J. Microsc.* (2019).